Transverse momentum dependent fragmentation functions from recent BELLE data

M. Boglione,[*] J. O. Gonzalez-Hernandez,[†] and A. Simonelli[‡]

Dipartimento di Fisica, Università di Torino, Via Pietro Giuria 1, 1-10125 Torino, Italy and INFN—Sezione Torino, Via Pietro Giuria 1, 1-10125 Torino, Italy

(Received 23 June 2022; accepted 29 September 2022; published 28 October 2022)

A new formalism for the factorization of the cross section for single-hadron production in e^+e^- annihilations, differential in z_h, P_T, and thrust, is applied to the phenomenological analysis of data recently measured by the BELLE Collaboration. Within this scheme the $e^+e^- \to hX$ cross section can be recast in the convolution of a perturbatively calculable coefficient and a universal transverse-momentum-dependent fragmentation function. While performing a next-to-leading-order calculation of the perturbative part of the process to next-to-leading logarithmic accuracy, we examine and thoroughly discuss the suitability of a number of possible *Ansätze* to model the nonperturbative part of this universal transverse-momentum-dependent fragmentation function, showing the extent to which present experimental data can actually constrain its shape and functional form in terms of z_h, P_T, and thrust.

DOI: 10.1103/PhysRevD.106.074024

I. INTRODUCTION

Transverse-momentum-dependent (TMD) parton distributions (PDFs) and fragmentation functions (FFs) are fundamental ingredients for the study of the inner structure of matter, as they encode how fundamental constituents bind into hadrons and shed light on the hadronization mechanism that, thanks to the confinement properties of QCD, leads to the formation of hadronic states. Their pivotal role in the investigation of the 3D structure of nucleons has motivated a huge effort in terms of experimental facilities as well as theoretical and phenomenological studies.

Unpolarized TMD PDFs are relatively well-known objects, as their extraction can rely on combined analysis of different processes, like semi-inclusive deeply inelastic scattering (SIDIS) and Drell-Yan scattering [1–5], for which dedicated TMD factorization theorems have been devised [6–9]. On the contrary, TMD FFs, their final-state counterparts, are rather less known. In fact, the study of unpolarized TMD FFs is currently based on the phenomenological analysis of the sole SIDIS, as data for e^+e^- annihilations into two hadrons, the ideal framework for their determination, are not yet available. To be precise, data on $e^+e^- \to h_1h_2X$ processes are only available for polarized TMD FFs, like the pion and kaon Collins function, or for the λ polarizing fragmentation function, for which several phenomenological studies have been performed; for example, some recent analyses can be found in Refs. [1,10–12]. Moreover, extractions relying on SIDIS cross sections are inevitably affected by the strong correlation between the TMD PDF and the TMD FF, which appear convoluted in the measured cross section. This issue could be circumvented by exploiting processes which involve only one TMD FF. In these regards, the thrust distribution of $e^+e^- \to hX$, sensitive to the transverse momentum of the detected hadron with respect to the thrust axis, as recently measured by the BELLE Collaboration [13], is a very promising candidate, as it represents a process in which the TMD effects are traced back to one single hadron, observed in the final state. The thrust axis is the direction $\vec{n}$ that maximizes the thrust T, defined as

$$T = \frac{\sum_i |\vec{P}_{(\mathrm{c.m.}),i} \cdot \hat{n}|}{\sum_i |\vec{P}_{(\mathrm{c.m.}),i}|}, \tag{1}$$

where the sum runs over all the detected particles in the c.m. frame. The variable T describes the topology of the final state, and it ranges from 0.5 to 1, where the lower limit corresponds to a spherical distribution of final-state particles, while the upper limit realizes a pencil-like event. In the following, the thrust axis will be identified with the axis of the jet to which the hadron h belongs, coinciding with

[*]mariaelena.boglione@unito.it
[†]joseosvaldo.gonzalezhernandez@unito.it
[‡]andrea.simonelli@unito.it

the direction of the fragmenting parton, eventually tilted by soft radiation recoil.

We note that some phenomenological analyses have been performed on $e^+e^- \to hX$ data [14–16], where some subsets of TASSO [17], PLUTO [18], MARKII [19], AMY [20], and CELLO [21] data, and the more recent BELLE [13] measurements have been considered. These studies ignored or only partially addressed issues related to universality and factorization properties of e^+e^- annihilations in a single hadron. From a theory perspective, in fact, the study of the $e^+e^- \to hX$ process has been very challenging, as standard TMD factorization techniques [6,7,22,23] do not apply.

As discussed in Refs. [24,25], the two-jet final-state topology of the above process can occur in three different kinematic configurations or "regions," denoted Regions 1, 2, and 3 in Refs. [24,25], each corresponding to a different factorization theorem. These kinematic regions can be defined in terms of the size of the transverse momentum P_T of the hadron observed inside the jet cone. If the hadron is detected very close to the thrust axis, the structure of the resulting factorization theorem is very similar to the standard TMD factorization, as in this case the soft radiation significantly affects the transverse momentum of the detected hadron. This configuration corresponds to Region 1, and it has recently been investigated for pion [26] and Λ [12,27] production, neglecting the thrust dependence, which is integrated out. On the other hand, if the hadron is detected very close to the jet boundary, its transverse momentum is large enough to affect directly the measured value of thrust. This configuration corresponds to Region 3. The associated factorization theorem involves a generalized fragmenting jet function (gFJF) rather than a TMD FF, and its treatment goes beyond the realm of TMD physics.

While Regions 1 and 3 are rather extreme configurations of the $e^+e^- \to hX$ phase space, the "bulk" of events will belong to Region 2, associated with the detection of hadrons with intermediate values of transverse momenta, neither extremely close to the thrust axis, nor too close to the jet external boundaries. Differently from the two above kinematic configurations, the proper theoretical treatment of Region 2 is still somehow controversial, as the two main available approaches on this subject, Refs. [24] and [25], do not find total agreement on the final form of the corresponding factorization theorem.

II. THEORETICAL FRAMEWORK

In this paper, we will follow the factorization scheme devised in Refs. [25,28,29], which offers some clear advantages for the practical implementation of a phenomenological analysis, leaving aside any discussion on the discrepancies between the two formalisms. These have been addressed in Sec. 5 of Ref. [25] and will be widely discussed in a forthcoming paper [30].

In Region 2, soft radiation does not contribute actively to the generation of TMD effects. This is what makes the standard TMD factorization crucially different from the factorization mechanism of Region 2, which shows features of both collinear and TMD factorization. The corresponding cross section can indeed be written as a convolution of a TMD FF with a "partonic cross section," encoding the details of thrust dependence. There are, however, two relevant issues that must be carefully taken into account. First of all, the TMD FF appearing in the $e^+e^- \to hX$ factorized cross section of Region 2 does not coincide with the usual TMD FF appearing in SIDIS cross sections. However, as we will discuss in more details below, differences between these two TMD definitions are well under control and their universality properties are not undermined [28]. Hence, a phenomenological analysis of the thrust distribution of $e^+e^- \to hX$ would allow us to access the genuinely nonperturbative behavior of a TMD FF, free from any soft radiation effects.

The second issue arises from the proper treatment of the rapidity divergences. Due to the very peculiar interplay between soft and collinear contributions, in Region 2 some of the rapidity divergences are naturally regulated by the thrust, T, but those associated with terms which are strictly TMD parts of the cross section need an extra artificial regulator, which is a rapidity cutoff in the Collins factorization formalism [6]. This induces a redundancy, which generates an additional relation between the regulator, the transverse momentum, and thrust. Such a relation inevitably spoils the picture in which the cross section factorizes into the convolution of a partonic cross section (encoding the whole T dependence) with a TMD FF (which encapsulates the whole P_T dependence), as both of these quantities turn out to depend on the rapidity cutoff. Hence, while the first becomes sensitive to the transverse momentum of the detected hadron, P_T, the other acquires a dependence on thrust, T. Moreover, the thrust resummation is intertwined with the transverse momentum dependence, making the treatment of the large-T behavior highly nontrivial.

A proper phenomenological analysis of Region 2 must rely on a factorized cross section where the regularization of rapidity divergences is properly taken into account. As usual, all the difficulties encountered in the theoretical treatment get magnified in the phenomenological applications. In this paper, we will adopt some approximations in order to simplify the structure of the factorization theorem without altering its main architecture. In particular, for single-pion production from e^+e^- annihilation, we refer to the cross section presented in Ref. [29]:

$$\frac{d\sigma}{dz_h dT d^2\vec{P}_T} = -\sigma_B N_C \frac{\alpha_S}{4\pi} C_F \frac{3+8\log\tau}{\tau} e^{-\frac{\alpha_S}{4\pi}3C_F\log^2\tau} \times \sum_f e_f^2 D_{1,\pi^\pm/f}(z_h, P_T/z_h; Q, \tau Q^2), \quad (2)$$

where z_h is the fractional energy of the detected pion, $\tau = 1 - T$, and $\sigma_B = 4\pi\alpha^2/3Q^2$ is the Born cross section. The unpolarized TMD FF, $D_{1,\pi^\pm/f}$, is defined in the impact parameter space, in terms of the transverse distance $\vec{b}_T$ Fourier conjugate of $\vec{q}_T \equiv \vec{P}_T/z_h$. At next-to-leading logarithmic (NLL) accuracy, and at the scales $\mu = Q$ and $\zeta = \tau Q^2$ as in Eq. (2), it reads [25]

$$\begin{aligned}\tilde{D}_{1,h/f}(z_h, b_{\mathrm{T}}; Q, \tau Q^2) &= \frac{1}{z_h^2}\left(d_{h/f}(z_h,\mu_{b_*}) + \frac{\alpha_S(\mu_{b_*})}{4\pi}\int_{z_h}^1 \frac{dz}{z}\left[d_{h/f}(z_h/z,\mu_{b_*}) z^2 C^{[1]}_{q/q}(z, b_*; \mu_{b_*}, \mu^2_{b_*}) + d_{h/g}(z_h/z,\mu_{b_*}) z^2 C^{[1]}_{g/q}(z, b_*; \mu_{b_*}, \mu^2_{b_*})\right]\right) \\ &\times \exp\left\{\log\frac{Q}{\mu_{b_*}} g_1(\lambda) + g_2(\lambda) + \frac{1}{4}\log\tau\left[g_2^K(\lambda) + \frac{1}{\log\frac{Q}{\mu_{b_*}}} g_3^K(\lambda)\right]\right\} M_{\mathrm{D}}(z_h, b_{\mathrm{T}}) \exp\left\{-\frac{1}{4} g_{\mathrm{K}}(b_{\mathrm{T}}) \log\left(\frac{Q^2}{M_H^2}\tau\right)\right\}, \end{aligned} \tag{3}$$

where the transition from small to large b_{T} has been treated through the b_* prescription by defining

$$b_*(b_{\mathrm{T}}) = \frac{b_{\mathrm{T}}}{\sqrt{1 + (b_{\mathrm{T}}/b_{\mathrm{max}})^2}}, \qquad \mu_{b_*} = \frac{2e^{-\gamma_E}}{b_*}, \tag{4}$$

as is usual in the Collins-Soper-Sterman formalism (CSS) [6,31,32].

Moreover, in order to ensure that integrating the above TMD FF renders the usual collinear FFs [indicated by lowercase d in Eq. (3)], we introduce in the b_* prescription a minimum value of b_{T}, b_{min}, as in Ref. [6], and replace Eq. (4) with $b_*(\sqrt{b_{\mathrm{T}}^2 + (b_{\mathrm{min}})^2})$. The first line of Eq. (3) embeds the unpolarized TMD FF at short distances and fixed scales $\mu = \mu_{b_*} \equiv 2e^{-\gamma_E}/b_*$ and $\zeta = \mu^2_{b_*}$. It is a standard result to express this contribution as an operator product expansion where the operator bases are the collinear FFs and the Wilson coefficients are fully predicted by perturbative QCD. The detailed expressions of the one-loop Wilson coefficients are given in the Appendix.

The second line of Eq. (3) describes the perturbative part of the evolution from $\mu = \mu_{b_*}$ to $\mu = Q$ and from $\zeta = \mu^2_{b_*}$ to $\zeta = \tau Q^2$. The functions g_i, $i = 1, 2$ and g_j^K, $j = 2, 3$ are required to reach the NLL accuracy. They depend on the variable $\lambda = 2\beta_0 a_S(Q)\log\frac{Q}{\mu_{b_*}}$. For convenience, they are reported in the Appendix.

Finally, the last line of Eq. (3) embeds the nonperturbative content of the unpolarized TMD FF, which is encoded in two nonperturbative functions that must be extracted from experimental data. The first is the model function M_{D}, which is the fingerprint of $D_{1,\pi^\pm/f}$ as it embeds the genuine large-distance behavior of the TMD. The second is the function g_{K}, describing the long-distance behavior of the Collins-Soper (CS) kernel, accounting for soft recoiling effects. Notice that a factor z_h is usually included [6] in the logarithm of g_{K}, which is not present in Eq. (3). This simply corresponds to a different choice for the reference scale of evolution. We choose not to include it in order to have a g_{K} factor completely unrelated to the z_h dependence in b_{T} space. With respect to the usual definition of TMDs [6,7], or the "square root definition" as labeled in Ref. [28], these two nonperturbative functions are related by the following equations:

$$M_{\mathrm{D}}^{\mathrm{sqrt}}(z_h, b_{\mathrm{T}}) = M_{\mathrm{D}}(z_h, b_{\mathrm{T}})\sqrt{M_{\mathrm{S}}(b_{\mathrm{T}})}, \tag{5a}$$

$$g_{\mathrm{K}}^{\mathrm{sqrt}}(b_{\mathrm{T}}) = \frac{1}{2} g_{\mathrm{K}}(b_{\mathrm{T}}), \tag{5b}$$

where M_{S} is the soft model introduced in Ref. [28], describing the nonperturbative content of the soft factor appearing in standard TMD factorization theorems. Notice that while M_{D} is different in the two definitions, g_{K} is basically the same, apart from a constant factor. Hence, for the extraction of g_{K} from Region 2 of $e^+e^- \to hX$, we can test the parametrization already used in past phenomenological extractions, based on standard TMD factorization. On the side of the TMD model, the comparison between the novel M_{D} extracted from Region 2 of $e^+e^- \to hX$ with its "square root" counterpart will shed light on the soft model $M_{\mathrm{S}}(b_{\mathrm{T}})$, the remaining unknown required to perform global phenomenological analyses.

The cross section in Eq. (2) can be obtained in two different ways. In Ref. [29], it is achieved by adopting a topology cutoff λ that forces the cross section to describe a two-jet final state in the limit $\lambda \to 0$. This introduces an additional artificial constraint which simplifies the computation of the transverse-momentum-dependent contributions by limiting the values of the transverse momentum to be smaller than the topology cutoff. Moreover, it allows us to set an explicit relation linking the thrust, T, to the rapidity cutoff ζ, namely $\zeta = \tau Q^2$. Finally, an approximated resummation of λ produces the exponential suppressing factor of Eq. (2), which replaces the effect of a proper thrust resummation [29]. Alternatively, Eq. (2) can be obtained from the correct factorization theorem of Region 2 devised in Ref. [25] by making two rather strong approximations. First, the whole transverse momentum

dependence encoded *outside* the TMD FF is integrated out up to the typical thrust-collinear scale $\sim\sqrt{\tau}Q$. This allows us to recover the naive picture of a partonic cross section convoluted with a TMD FF. Then, the TMD is equipped with a rapidity cutoff, set to the minimal allowed rapidity for particles belonging to the same jet of the detected hadron, corresponding to $\zeta = \tau Q^2$. In this way, the underlying correlation between thrust and transverse momentum (due to the peculiar role of the rapidity regulator in Region 2) is strongly simplified. Nevertheless, Eq. (2) embodies the essence of Region 2, as the definition of the TMD FF is not affected by nonperturbative soft effects. Moreover, it represents the first attempt to account for the interplay between thrust and the rapidity regulator. In this paper, we present the first extraction of this universal TMD FF from $e^+e^- \to hX$ data by the BELLE Collaboration [13], belonging to Region 2, within the specific framework of Refs. [25,29].

III. PHENOMENOLOGY

In order to use Eq. (2), complemented by the definition of unpolarized TMD FF in Eq. (3), one must choose parametric forms for M_{D} and g_{K}, which describe the nonperturbative behavior of the TMD. Such choices are generally affected by the kinematical region of the data under consideration. This poses a big challenge, since the error estimation of factorization theorems in QCD does not allow for sharp boundaries to be drawn. For instance, the small-q_{T} cross section in Eq. (2) and its associated error of $O(q_{\mathrm{T}}^2/Q^2)$ do not imply that the formalism should describe the data up to $q_{\mathrm{T}} \sim Q$, but rather that in this region issues describing the data are to be expected. With no further indication of how far one can extend the description into the larger-q_{T} region, one is left with model-dependent phenomenological results as the only indication of the validity of the formalism. An algorithm to delineate the contours of $e^+e^- \to hX$ kinematic regions where specific factorization regimes can be applied was developed in Ref. [25], which we will refer to in our analysis. Another delicate point is the choice of collinear fragmentation functions. While one expects part of the z dependence of theory lines to come from the behavior of the collinear FFs, there is no restriction regarding a possible z dependence in the function M_{D}. Again, how appropriate a given set is depends on the parametric form of the model. In the following sections, we systematically explain our choices.

For our study, we will use a simple minimization procedure of the χ^2 given by

$$\chi^2 = \sum_{j=1}^{n} \frac{(T_j(\{p\}) - E_j)^2}{\sigma_j^2}, \tag{6}$$

with $\{E_j\}$ being the set of the n data points under consideration, and where the corresponding theory computations $\{T_j\}$ depend on a set $\{p\}$ of m parameters. The uncertainties σ_j are treated as independent uncorrelated errors—i.e., different sources of errors provided by the BELLE dataset are added in quadrature. Future refinements of our work can be achieved by modifying the definition in Eq. (6) in order to account for the correlations in the systematic uncertainties. This, however, requires more detailed information about the different sources of such types of errors, which is not available. For now, we proceed by minimizing Eq. (6) as done in previous related analyses [15,26,27,33,34].

In order to test goodness of fit, we use the χ^2 per degree of freedom, given by $\chi^2_{\mathrm{d.o.f.}} = \chi^2/(n-m)$, which should be close to unity for a model to be considered appropriate. We will estimate the statistical errors of our analysis by determining 2σ confidence regions based on a straightforward application of the Neyman-Pearson lemma and Wilks's theorem. Concretely, provided a minimal set of parameters $\{p_0\}$ with χ^2_0, we consider parameter configurations $\{p_i\}$, with χ^2_i given by

$$\chi^2_i < \chi^2_0 + \Delta\chi^2, \tag{7}$$

where $\Delta\chi^2$ is *not* an arbitrary tolerance but rather depends on the confidence level and the number of parameters varied. For the $c\,\sigma$ confidence level, one has

$$\mathrm{erf}\left(\frac{c}{\sqrt{2}}\right) = \int_0^{\Delta\chi^2} dx\, X^2_D(x), \tag{8}$$

with $X^2(D)$ being a chi-squared distribution with D degrees of freedom equal to the number of parameters varied.[1]

A. TMD FF z dependence and choice of collinear FFs

Similarly to the usual CSS formalism for two-hadron production, the impact parameter space in Eq. (3) is constrained at small b_{T} by a small-distance OPE, hence the appearance of the convolution of collinear FFs with matching coefficients $\mathcal{C}$, which we denote by $d \otimes \mathcal{C}$. This factor provides an important constraint of the z_h dependence for the TMDs. As discussed before, the transition from short to large distance of the TMD is regulated by the b_* prescription, for which a maximum value or "freezing point" must be set, below which one expects perturbation theory to apply. Such a maximum distance, b_{max} in Eq. (4), corresponds to a minimum perturbative scale of $\mu_{\mathrm{min}} = 2e^{-\gamma_E}/b_{\mathrm{max}}$. For our studies, we choose $b_{\mathrm{max}} = 1.0\ \mathrm{GeV}^{-1}$, which ensures that perturbative quantities are never evaluated below a scale of 1.12 GeV. This seems like a sensible

[1]This equation gives $\Delta\chi^2 = 1$ for 1σ C.L. when varying only one parameter. We consider 2σ and mostly vary all parameters at once, so $\Delta\chi^2$ values will be larger than unity.

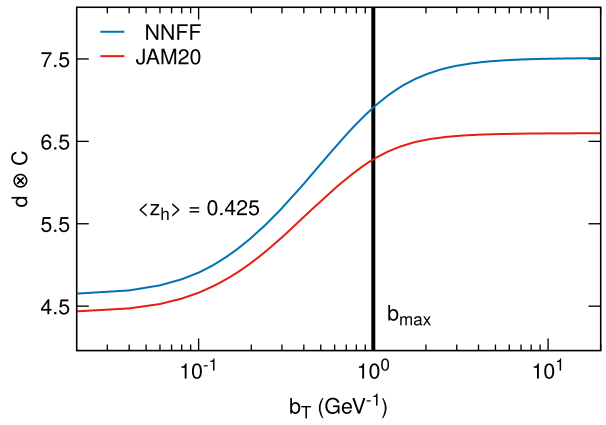

FIG. 1. Convolution of the collinear fragmentation function and matching coefficients, $d \otimes \mathcal{C}$, for the NNFF [33] and JAM20 [35] sets. Here z_h is fixed at $z_h = 0.425$, but significant differences can also be observed at other values of z_h.

choice, since perturbation theory is known to work well in collinear observables down to a scale of around 1.0 GeV.

With this choice, we turn to the question of choosing a set of collinear FFs. We will compare the NNFF [33] and the JAM20 [35] next-to-leading-order (NLO) sets.[2] These are modern analyses that represent the state of the art in collinear FF extractions and are readily available through LHAPDF [36]. As it can be seen in Fig. 1, the computation of $d \otimes \mathcal{C}$ may render significantly different results for each collinear FF set. One may suspect that the extraction of the TMD is sensitive to the choice of collinear functions. It is, however, not obvious that either of the collinear sets is to be preferred over the other. It is entirely possible that by adjusting values of the model parameters for say, $M_{\rm D}$, a similar description of the data could be achieved with the two collinear FF sets. By any consideration, the question of which set is more appropriate depends on the choices of the model.

In order to choose a set, we perform preliminary fits at fixed values of $T = 0.875$ and look for the one that better describes the data, in terms of the minimal $\chi^2_{\rm d.o.f.}$. We consider for now only the kinematical ranges $0.375 < z_h < 0.725$ and $q_{\rm T}/Q < 0.20$. This includes enough data points to constrain the tests. At this stage, we only attempt to parametrize $M_{\rm D}$ and set the exponential factor containing $g_{\rm K}$, in the last line of Eq. (3), equal to unity.

Notice that according to Ref. [25], data corresponding to z_h bins with $z_h \leq 0.375$ would be dominated by Region 1, which requires a different factorization theorem. For this reason, we do not consider them here.

In a first attempt to test the collinear functions, one may consider models for $M_{\rm D}$ with no explicit z_h dependence and perform fits for fixed values of z_h. The choice of models is summarized in the top two entries of Table I: model 1 is inspired by a Gaussian-like $b_{\rm T}$ behavior; while model 2, proportional to a modified Bessel function of the second kind, corresponds to a power law in momentum space and is the same functional form considered for $M_{\rm D}$ in Ref. [29]. As can be seen in Fig. 2, these models result in rather high values of $\chi^2_{\rm d.o.f.}$, giving a bad description of the data. Nonetheless, it is noteworthy that the $\chi^2_{\rm d.o.f.}$ tends to be larger for the JAM20 set. Both models seem to work at $q_{\rm T}/Q < 0.1$ but deteriorate fast for $0.1 < q_{\rm T}/Q < 0.2$. In the following subsections, we will set our final $q_{\rm T}$ cut to the intermediate value $q_{\rm T}/Q < 0.15$. For now, we will leave this aside and continue to address the z_h dependence. Recall that so far, we have performed only independent fits

TABLE I. Models in impact parameter space used for preliminary tests in this section. The first two entries correspond to z_h-independent models for $M_{\rm D}$. Models labeled as "BK" are proportional to a modified Bessel function of the second kind and correspond to a power law in momentum space. Entries three and four are z_h-dependent models for $M_{\rm D}$, obtained by modifying the mass parameter of the BK model, as indicated. The last entry introduces z_h dependence to the BK model by a multiplicative factor with Gaussian behavior in $b_{\rm T}$.

ID	$M_{\rm D}$ model	Parameters
	z_h-independent models	
1) Exp-p	$e^{-(M_0 b_{\rm T})^p}$	M_0, p
2) BK	$\frac{2^{2-p}(b_{\rm T}M_0)^{p-1}}{\Gamma(p-1)} K_{p-1}(b_{\rm T}M_0)$	M_0, p
	z_h-dependent models	
3) BK-1	$M_0 \to M_1(1-\eta_1 \log(z_h))$	M_1, η_1, p
4) BK-2	$M_0 \to M_2(1+\frac{\eta_2}{z_h^2})$	M_2, η_2, p
5) BK-g	$e^{(M_g b_{\rm T})^2 \log(z_h)} \times$ BK	M_g, M_0, p

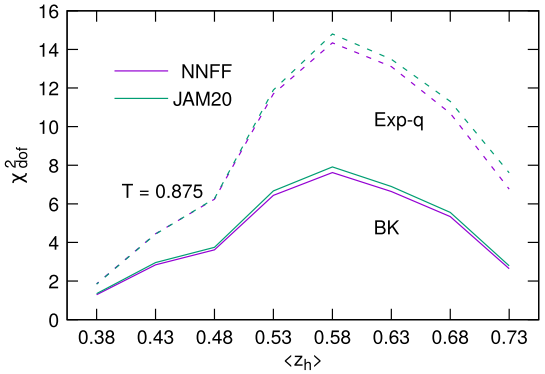

FIG. 2. Minimal $\chi^2_{\rm d.o.f.}$ for fits at fixed $T = 0.875$ and individual z_h bins in the range $0.375 < z_h < 0.725$, for $M_{\rm D}$ models with no z_h dependence. Here, $q_T/Q < 0.20$. Dashed and solid lines correspond to the first and second entries in Table I, respectively. For each model, we have two parameters and a total of nine individual fits, one per z_h bin. Note that even with such large values of $\chi^2_{\rm d.o.f.}$, the mild relative differences between using JAM20 and NNFF suggest that either set could describe the data to the same quality.

[2]Note that we use a recent update of the JAM20 pion FFs, obtained from https://github.com/QCDHUB/JAM20SIDIS.

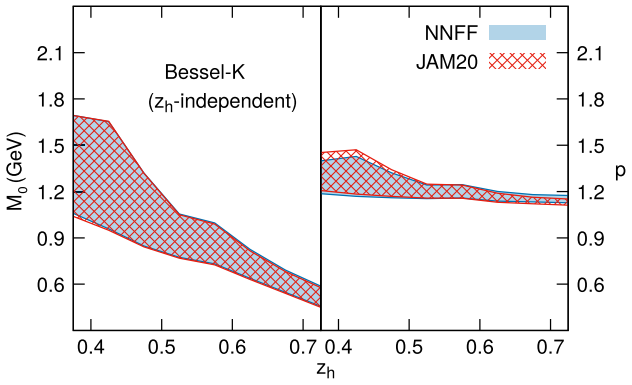

FIG. 3. Minimal parameter values for fits at fixed $T = 0.875$ and individual z_h bins in the range $0.375 < z_h < 0.725$, for the $M_{\rm D}$ model in the second entry of Table I (z_h-independent BK model). Here, $q_T/Q \leq 0.20$. Results correspond to the solid lines in Fig. 2. In this case, where we fit z_h bins separately, the incompatibility of M_0 and p for different z_h's suggests that a z_h dependence is needed if the model is to describe the data on a simultaneous fit of the $0.375 < z_h < 0.725$ range. It is interesting to note that the dimensionful parameter M exhibits a stronger correlation to z_h.

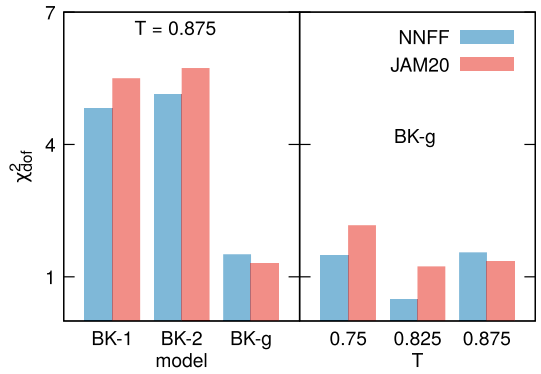

FIG. 4. Minimal $\chi^2_{\rm d.o.f.}$ for fits in the kinematic range $0.375 < z_h < 0.725$ (z_h bins are fitted simultaneously), for the z_h-dependent models for $M_{\rm D}$ in the last three entries of Table I. Here, $q_T/Q \leq 0.20$. Left panel: comparison of the results obtained with NNFF [33] and JAM20 [35] for fixed $T = 0.875$. Right panel: fixed-T fits for $T = \{0.750, 0.825, 0.875\}$, using the BK model with a Gaussian z_h-dependent term (last entry in Table I). Similarly to the results presented in Fig. 2, the NNFF set consistently produces smaller values of $\chi^2_{\rm d.o.f.}$.

at fixed $T = 0.875$, and separately for each bin inside the range $0.375 < z_h < 0.725$. A useful exercise is to plot the values of the resulting minimal parameters in terms of z_h, as is done in Fig. 3, for the BK model. There, it is clear that if one expects to fit all bins in z_h simultaneously (still at fixed $T = 0.875$), some z_h dependence shall be needed in the parametric form for $M_{\rm D}$. We remark that an important result of the factorization scheme is that $g_{\rm K}$ must be independent of z_h. Another interesting aspect of Fig. 3 is that a stronger z_h dependence is observed for the mass parameter M_0 than for the dimensionless parameter p. We find that improving the trend of theory lines in the variable z_h is more readily done by introducing a z_h dependence in dimensionful parameters. We have observed this for several cases we tested, although here we only show a few of them. More generally, one could expect strong correlation between all parameters in $M_{\rm D}(b_{\rm T})$. For instance, a closer inspection of the example in Fig. 3 shows that the two parameters shaping the $b_{\rm T}$ profile of $M_{\rm D}$, M_0 and p, display a similar trend as a function of z_h. We will come back to this later on in the next sections.

We attempt three different z_h-dependent models for $M_{\rm D}$, as indicated in the last three entries of Table I. The first two are modifications of the BK model, where we modify the mass parameter as $M_0 \to M(z)$, adding in each case one more parameter to introduce, respectively, a logarithmic and a power term in z_h. The last one is the BK model multiplied by $z_h^{(M_g b_{\rm T})^2}$, so that the z_h dependence is controlled by this additional multiplicative function and determined by the mass parameter M_g.

Results for these three models can be seen in the left panel of Fig. 4. Despite the large values of $\chi^2_{\rm d.o.f.}$ for the first two models, we find a considerable improvement with respect to the z_h-independent BK model. The third model works indeed much better, which is due partly to its z_h dependence but also to the Gaussian behavior introduced by the factor $z_h^{(M_g b_{\rm T})^2}$. The Gaussian behavior of this model improves the description at the large end of the selected range of $q_{\rm T}$, giving much lower values of $\chi^2_{\rm d.o.f.}$. For this last model, the last entry in Table I, we perform two more fixed-T fits for $T = 0.750$ and $T = 0.825$, resulting in χ^2's roughly 3 times smaller than those corresponding to models BK1 and BK2. Results are shown in the right panel of Fig. 4.

One should be careful to interpret these results. First, while it may seem that the last model should be the obvious choice to extract the unpolarized TMD FF, the other two z_h-dependent models we have considered here are able to describe the data well up to $q_{\rm T}/Q < 0.1$, as we will show in the following subsections. This is a delicate point, since one does not know *a priori* for which maximum value of $q_{\rm T}/Q$ one can still trust that the errors $O((q_{\rm T}/Q)^2)$ of Eq. (3) are small enough so that the formalism is still valid. For instance, if the cut on $q_{\rm T}/Q$ was made more restrictive, say $q_{\rm T}/Q < 0.1$, the clear advantage of the Gaussian z_h-dependent model, describing the data in the region $0.1 < q_{\rm T}/Q < 0.2$, would become less significant.

We close our preliminary discussion of the z_h dependence by stating the main conclusions of this subsection. First, a stronger z_h dependence is observed in mass parameters than in dimensionless parameters. This is an observation that applies to several models we tested, of which we provide one concrete example in Fig. 3. In the specific case of Fig. 3, we also find that z_h may strongly correlate the model parameters M_0 and p. Second, in all the

preceding discussions, and despite inadequacies in some of the models considered, $\chi^2_{\text{d.o.f.}}$ values tend to be smaller with NNFF, so this will be our choice for our main analysis, but we will not yet be set on a specific model for M_{D}. Based on our preliminary studies of this section, we expect that using JAM20 would give larger values of $\chi^2_{\text{d.o.f.}}$, although not by much.

B. Behavior of the unpolarized TMD FF in the large-b_{T} limit

In this subsection, we will address the behavior of the unpolarized TMD FF in impact parameter space. Specifically, we look at possible parametric forms for M_{D} in Eq. (3), paying special attention to the large-b_{T} limit. For the purposes of our discussion, we identify two different possible meanings for "large-b_{T}" behavior:

(1) Asymptotically large b_{T}.
(2) The maximum b_{T} accessible through data.

The first one corresponds to the formal limit $b_{\text{T}} \to \infty$, in which one may write asymptotic expansions for a known parametric form. For instance, the BK model discussed in the previous subsection has an asymptotic limit

$$\frac{2^{2-p}(b_{\text{T}}M_0)^{p-1}}{\Gamma(p-1)} K_{p-1}(b_{\text{T}}M_0) \to \sqrt{\pi}\frac{2^{\frac{3}{2}-p}(b_{\text{T}}M)^{p-\frac{3}{2}}}{\Gamma(p-1)} e^{-b_{\text{T}}M_0} \tag{9}$$

characterized by an exponentially decaying behavior as $b_{\text{T}} \to \infty$. The second one, instead, refers to the largest region in b_{T} that is accessible phenomenologically—i.e., the largest distances at which the data can constrain the model, which can be better determined after carrying out a data analysis. The largest b_{T} accessible phenomenologically corresponds to the case of measurements at values of Q small enough that nonperturbative effects are maximized, but large enough that TMD factorization still holds. Even at scales of, say, $Q = 2$ GeV, it is possible that the asymptotic behavior of the TMDs cannot be resolved completely. At BELLE kinematics, where $Q \approx 10$ GeV, it is unlikely that one can find strong constraints for the asymptotic behavior of TMDs.

This would mean that fitting BELLE data may be possible with parametric forms of distinct asymptotic behavior. However, when considering data at smaller energy scales, for which the maximum b_{T} accessible is likely larger than that at BELLE energies, one may find inconsistencies in a global fit if the asymptotic behavior of b_{T} is not chosen appropriately. Theoretical constraints are important in light of all these issues encountered at lower-energy phenomenology—see, for example, Refs. [37–43]. To do so, we follow some of the considerations made in Ref. [44]. Thus, for this work we will look for a parametric M_{D} that in b_{T} space decays exponentially, but that is able to describe BELLE data at least as well as model 5 in Table I, which in the preliminary cases considered so far, seems to be suitable. A possible candidate is shown in Table II, where for convenience we have explicitly rewritten model 5 of Table I. Both models in Table II correspond to a powerlike behavior in momentum space, characterized in b_{T} space by the modified Bessel function of the second kind, times an extra factor which we denote as F. To make the comparison between exponential and Gaussian asymptotic behavior more transparent, in this preliminary study we consider only the models in Table II. Note that even in the case $F = 1$, one may recover an exponentially decaying behavior asymptotically, from the Bessel function alone, as seen in Eq. (9). We will consider this case later, as it requires a detailed explanation of possible final parametric forms, which account for the strong correlations of parameters in M_{D} related to the z_h dependence, as noted in the previous subsection.

TABLE II. Models for M_{D} in impact parameter space. Both cases shown are obtained by multiplying the model BK of Table I, which corresponds to a power law in momentum space, by an additional function of b_{T} and z_h.

$M_{\text{D}} = \frac{2^{2-p}(b_{\text{T}}M_0)^{p-1}}{\Gamma(p-1)} K_{p-1}(b_{\text{T}}M_0) \times F(b_{\text{T}}, z_h)$		
$M_z = -M_1 \log(z_h)$		
ID	F model	Parameters
I	$F = \left(\frac{1+\log(1+(b_{\text{T}}M_z)^2)}{1+(b_{\text{T}}M_z)^2}\right)^q$	$M_0, M_1, p, q = 8$
IG	$F = \exp((M_g b_{\text{T}})^2 \log(z_h))$	M_0, M_g, p

For now, we will compare how well the models in Table II may describe the data. Our aim is to provide a practical example where two models that describe the data reasonably well are not necessarily constrained in the asymptotically large-b_{T} limit. Decoupling the question of what is an appropriate parametric form for the P_{T} behavior of M_{D} is not independent of the choices to model its z_h dependence. Thus, we proceed as follows. First, we perform three fits at fixed values of $T = \{0.750, 0.825, 0.875\}$, where in each case, we include BELLE data in the region $q_{\text{T}}/Q < 0.20$ and $0.375 < z_h < 0.725$. To

TABLE III. Minimal $\chi^2_{\text{d.o.f.}}$ resulting from fitting the two parametric forms for M_{D} in Table II. In each case, we perform three independent fits, one for each value $T = \{0.750, 0.825, 0.875\}$, in the ranges $q_{\text{T}}/Q < 0.2$ and $0.375 < z_h < 0.725$. As far as the description of the data is concerned, all three cases seem to be acceptable; see explanation in the text.

	$\chi^2_{\text{d.o.f.}}$ (fixed-T fits)		
M_{D} model	$T = 0.750$	0.825	0.875
I	1.20	0.38	1.02
IG	1.46	0.47	1.51

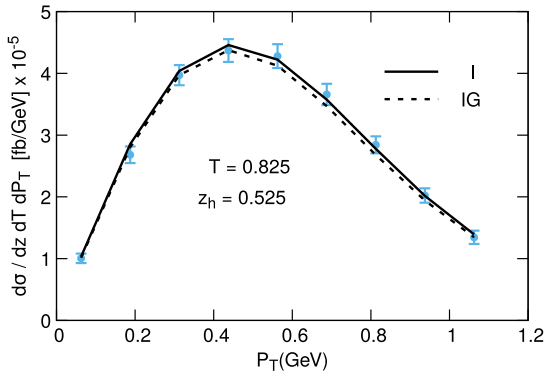

FIG. 5. Best-fit lines for both models in Table II, obtained by fitting BELLE data for the kinematics $T = 0.825$, $0.375 < z_h < 0.725$, and $P_T/z_h Q < 0.2$. Note that both lines follow essentially the same profile in the region of the data shown.

accommodate the z_h dependence, we choose a logarithmic behavior in the function F as shown in Table II. Since we are not fitting the three T bins simultaneously, we will not be able to also fit g_K, which correlates to thrust, so for now we set $g_K = 0$. Then, we will look at a single case—one value of T and z_h—where the P_T dependence is described well by both models, and look at the results in P_T and b_T space.

The results of the fixed-T fits are shown in Table III. The smaller values of $\chi^2_{\text{d.o.f.}}$ obtained with model I are related to the choice $q = 8$, which allows for a good description of the z_h bins considered. Note that modifying the z_h behavior in model IG could improve its best fit $\chi^2_{\text{d.o.f.}}$ as well. At this stage, we consider both models as candidates to parametrize M_D, since our main interest is to discuss the P_T dependence.

Now we look at the case $z_h = 0.525$ and $T = 0.825$, for which both models describe the data reasonably well. In fact, as seen in Fig. 5, the models of Table II have the same profile and almost lie on top of each other. Corresponding lines in b_T space are shown in Fig. 6, where it can be seen that for values $b_T > 4$ GeV^{-1}, the cross sections calculated using models I and IG deviate. This is, of course, due to the differences in the asymptotic behavior of the models. This example simply illustrates that the asymptotic behavior of the TMD FF is not necessarily constrained by BELLE data after some large value of b_T. However, the reason to prefer an asymptotic behavior like that of model I comes from the necessity to fit data at lower energies in the future, for which the large-b_T Gaussian falloff may not be appropriate.

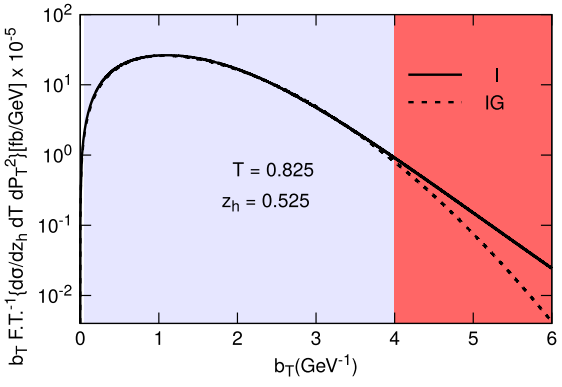

FIG. 6. Best-fit lines for both models in Table II in b_T space, obtained by fitting BELLE data for the kinematics $T = 0.825$, $0.375 < z_h < 0.725$, and $P_T/z_h Q < 0.2$. Lines correspond to those in Fig. 5. The deviation of the two theory lines after $b_T > 4$ GeV^{-1} indicates the lack of sensitivity to the asymptotic behavior of the models in this particular example.

From here on out, we will focus on models for M_D that decay exponentially in the asymptotically large-b_T limit. More precisely,

$$\log(M_D) \underset{b_T \to \infty}{\sim} -C\, b_T + o(b_T), \tag{10}$$

with C being a positive mass parameter, and where we have used the lowercase o symbol to indicate sublinear terms in b_T. Furthermore, we will explore two different approaches, leading to two classes of models. The first one is model I in Table II, which corresponds to the function of Eq. (9) times the z_h-dependent function F. The second one is similar to model I but sets $F = 1$ and models the z_h dependence through both the mass parameter M_0 and the power p of the Bessel function of Eq. (9).

Before performing our extraction, however, we need to set a parametric form for g_K.

C. Behavior of g_K in the large-b_T limit

The usual definition of the TMD FF in the CSS formalism differs from that introduced in Ref. [28] by a nonperturbative function $M_S(b_T)$, as explained in Sec. II and given in Eq. (5a). $M_S(b_T)$ is associated with soft gluon effects and originates from the fact that in the latter definition the TMDs are purely collinear objects, while in the CSS definition soft radiation contributions are included in the TMD definition itself. This means that the nonperturvative function $M_D(b_T)$ introduced in Eq. (2) and discussed in Sec. II cannot be used directly in e^+e^- two-hadron production or SIDIS processes; see Eq. (5a). Note, however, that the nonperturbative function g_K has been defined to be the same as in the usual CSS formalism, up to a trivial factor of 2; see Eq. (5b). Thus, it characterizes the large-distance behavior of the Collins-Soper kernel as defined in Ref. [6]. This is perhaps one of the most useful aspects of the formalism in Refs. [25,28,29,45] in the context of global fits, since it allows for comparisons of the extracted g_K with other recent work (see, for example, Refs. [3,4,46,47]). In order to choose a suitable parametrization for g_K, we use the following observation as a guiding principle:

In general, one may write the TMD FF in b_T space as

$$\tilde{D}(b_T,\zeta) = \tilde{D}(b_T,\zeta_0)\exp\left\{-\frac{g_K}{4}\log\left(\frac{\zeta}{\zeta_0}\right)\right\}(\cdots), \tag{11}$$

where only the dependence on b_T and ζ has been written explicitly, and the ellipsis indicates other terms containing perturbatively calculable quantities. Using the hypothesis in Eq. (10), one has that in the large-b_T limit,

$$\log\left(\tilde{D}(b_T,\zeta)\right) \overset{b_T\to\infty}{=} -Cb_T - \frac{g_K^{\text{large } b_T}}{4}\log\left(\frac{\zeta}{\zeta_0}\right) + o(b_T). \tag{12}$$

We then note that

$$g_K \overset{b_T\to\infty}{=} o(b_T) \Rightarrow \log(\tilde{D}(b_T,\zeta)) = O(b_T), \tag{13}$$

independently of ζ and ζ_0. This seems like a reasonable condition, since ζ_0 is a somewhat arbitrary reference scale: for instance, it could be chosen depending on the kinematics of a particular phenomenological analysis. We will consider in this analysis only the hypothesis that asymptotically $g_K = o(b_T)$. As a counterexample, with the same ansatz for the asymptotic behavior of $\tilde{D}(b_T,\zeta)$, Eq. (10), choosing the large-b_T behavior of g_K to be quadratic would implicitly assign a special role to the reference scale ζ_0, in the sense that in this case for $\zeta = \zeta_0$, $\log(\tilde{D}(b_T,\zeta)) = O(b_T)$, while for $\zeta \neq \zeta_0$, $\log(\tilde{D}(b_T,\zeta)) = O(b_T^2)$. Note that one could set g_K to be $O(b_T)$ instead of $o(b_T)$ and still have Eq. (13) be valid. However, this allows for $\tilde{D}(b_T,\zeta)$ to be divergent in the limit $b_T \to \infty$, for sufficiently small ζ/ζ_0 (see also the discussion in Ref. [44]). Note that a sublinear b_T behavior for g_K has already been suggested by several authors—see, for instance, Eq. (79) in Ref. [44], Eq. (40) in Ref. [48] and Eq. (24) in Ref. [49]).

Our analysis will be conducted by adopting the following functional forms for the large-b_T behavior of g_K:

$$g_K \overset{b_T\to\infty}{\sim} \log(M_K b_T), \tag{14}$$

$$g_K \overset{b_T\to\infty}{\sim} (M_K b_T)^{(1-2p_K)} \qquad 0 < p_K < 1/2, \tag{15}$$

where the first expression is similar to that considered in Ref. [48], while the second expression corresponds to the model calculation presented in Ref. [49] for the CS kernel as $b_T \to \infty$ (but with an undetermined power p_K). Here, M_K is a free parameter with mass dimensions which helps in shaping the b_T dependence of g_K. We have also considered a constant asymptotic form, as suggested in Ref. [38], but, limited to the data sample we are presently fitting, we obtain consistently larger χ^2's compared to those obtained using a sublinear asymptotic behavior for g_K.

We stress that our main purpose is to test whether or not $g_K = o(b_T)$ as $b_T \to \infty$ is a suitable asymptotic dependence for the nonperturbative behavior of the Collins-Soper kernel. In this sense, Eqs. (14) and (15) should be seen only as a proxy for such a hypothesis. The consideration of two models for g_K will allow us to get a "measure" of the correlations between M_D and g_K, and of the theoretical uncertainties introduced by model choices.

D. Behavior of g_K in the small-b_T limit

There is a general consensus that the behavior of g_K in the small-b_T limit should be powerlike—see, for example, Refs. [4,44,47–50]. Often, phenomenological studies have assumed

$$g_K \overset{b_T\to 0}{\sim} c_1 b_T^2. \tag{16}$$

For instance, Ref. [4] uses

$$g_K = c_1 b_T^2 + c_2 b_T^4, \tag{17}$$

where a strong suppression at small b_T is necessary to reach a satisfactory description of Drell-Yan data at extremely large energies, which require high accuracy in the perturbative and logarithmic expansion. For this analysis, where the perturbative expansion only extends to NLL, we start by testing two different models for g_K which ensure a b_T^2 behavior at small b_T, while respecting the asymptotic trends discussed above. More specifically, we look at the following functional forms:

$$c\log(1 + (M_K b_T)^2), \tag{18}$$

$$a b_T^{p_k}(1 - e^{-b/a b_T^{(2-p_k)}}). \tag{19}$$

Both models show some drawbacks. First of all, the parameter space is not well constrained. Moreover, larger values of χ^2 point to the inadequacy of the power 2 for b_T. In fact, in our preliminary tests, we find that our fit is rather sensitive to the modulation of g_K in the large-b_T region. Remarkably, it shows a strong preference for a sublinear power or logarithmic rising of g_K, while definitely ruling out the b_T^2 or b_T^4 behavior at large b_T. Indeed, it is likely that increased perturbative accuracy could accommodate for the behavior of Eq. (16) at small b_T. We therefore relax the constraint that g_K should go to zero quadratically in the small-b_T limit by simply requiring it to go to zero as some generic power $p_K > 0$. This will also allow us to reduce the number of free parameters for our final analysis. Thus, we will focus on the following parametrizations:

$$g_K = \log(1 + (M_K b_T)^{p_K}), \tag{20}$$

TABLE IV. Models for $M_{\rm D}$ and $g_{\rm K}$ in impact parameter space for our main analysis. $M_{\rm D}$ is obtained by multiplying the BK model, which corresponds to a power law in momentum space, with an additional function of $b_{\rm T}$ and z_h.

$M_{\rm D} = \frac{2^{2-p}(b_{\rm T}M_0)^{p-1}}{\Gamma(p-1)} K_{p-1}(b_{\rm T}M_0) \times F(b_{\rm T}, z_h)$		
ID	$M_{\rm D}$ model	Parameters
I	$F = \left(\frac{1+\log(1+(b_{\rm T}M_z)^2)}{1+(b_{\rm T}M_z)^2}\right)^q$ $M_z = -M_1 \log(z_h)$	M_0, M_1 $p = 1.51$, $q = 8$
II	$F = 1$ $M_z = M_\pi \frac{1}{z_h f(z_h)^2} \sqrt{\frac{3}{1-f(z_h)}}$ $p_z = 1 + \frac{3}{2}\frac{f(z_h)}{1-f(z_h)}$ $f(z_h) = 1-(1-z_h)^\beta$, $\beta = \frac{1-z_0}{z_0}$	z_0
	$g_{\rm K}$ model	
A	$g_{\rm K} = \log(1 + (b_{\rm T}M_{\rm K})^{p_{\rm K}})$	$M_{\rm K}$, $p_{\rm K}$
B	$g_{\rm K} = (M_{\rm K} b_{\rm T})^{(1-2p_{\rm K})}$	$M_{\rm K}$, $p_{\rm K}$

$$g_{\rm K} = (M_{\rm K} b_{\rm T})^{(1-2p_{\rm K})} \qquad 0 < p_{\rm K} < 1/2. \tag{21}$$

The functional forms in Eqs. (20) and (21), labeled A and B, respectively, are summarized in Table IV. They optimize the quality of the fit while keeping the number of free parameters under control.

E. Final models and data kinematics

For our main analysis, we use the BELLE data for pion production with the weak decay subtracted out. Furthermore, no integration on bin sizes is performed; we consider the midpoint value of each bin in the ranges

$$0.375 \le z_h \le 0.725, \qquad 0.750 \le T \le 0.875, \tag{22}$$

corresponding to Region 2 (see Ref. [25]). Furthermore, as the TMD formalism of Refs. [25,29] regards the region in which $q_{\rm T} = P_{\rm T}/z_h \ll Q$, we adopt the cut

$$q_{\rm T}/Q \le 0.15, \tag{23}$$

which gives us some confidence that the appropriate collinear TMD factorization theorem is applied, and we perform a standard χ^2 minimization procedure for each one of the models summarized in Table IV. More restrictive cuts make it difficult to find an optimal solution, while less stringent ones result in large values of χ^2.

As mentioned before, for our analysis we consider two different models for each $M_{\rm D}$ and $g_{\rm K}$, in order to provide a reliable estimation of the uncertainties affecting the extraction of the TMD FF. For $g_{\rm K}$, we consider the functional forms in Eqs. (20) and (21), which we call models A and B, respectively. For $M_{\rm D}$, our starting point is the Fourier transform of a power law in momentum space, taking into account that a z_h dependence is necessary for a successful description of the BELLE cross sections [13]. These two models, labeled I and II, differ only in the treatment of the z_h dependence. In total, we have four different cases we will use, which we label as models IA, IB, IIA, and IIB.

1. Models IA and IB

Model I for $M_{\rm D}$ was already introduced in Sec. III B (see Table II) and, as summarized in Table IV, it concentrates the full z_h dependence of $M_{\rm D}$ within the extra $F(b_{\rm T}, z_h)$ factor, which is controlled by the mass parameter $M_z = -M_1 \log(z_h)$, while the Bessel function and other factors corresponding to the power law in momentum space only depend on $b_{\rm T}$.

Thus, models IA and IB have initially six parameters each. In both cases, we find that when trying to fit all of the parameters simultaneously, some are poorly constrained and/or show very strong correlations. This may indicate some "redundancy"—i.e., the existence of nonindependent parameters. This can be an issue when attempting to provide a transparent statistical interpretation of results. We find that we have to fix a total of three parameters—two for $M_{\rm D}$ and one for $g_{\rm K}$—in order to avoid such a situation. We choose to fix the dimensionless powers, p, q, and $p_{\rm K}$, so that we will find best-fit values of parameters that may have the interpretation of a "typical mass" of the observables. First, we set $p = 1.51$, so that the derivative of the Bessel function in model I vanishes at $b_{\rm T} = 0$; this prevents $M_{\rm D}$ from being sharply peaked at $b_{\rm T} = 0$. After setting the value for p, we find that the minimum[3] value of χ^2 that one can obtain (for both models IA and IB) corresponds to $q \approx 8$, so we fix $q = 8$. Finally, provided these choices for p and q, we perform a fit in order to obtain the optimal values for the power parameter $p_{\rm K}$ for each model IA and IB. We show the results of this last step in Fig. 7 for model IA (fixed $p = 1.51$, $q = 8$, and varying $p_{\rm K}$) in order to illustrate the need to fix some of the parameters. There, the circles display parameter configurations i with χ_i^2 values that deviate from the minimum χ_0^2 by no more than a "tolerance"[4] $\Delta\chi^2 = 9.72$; green dots represent the minimal configuration. While in this case it is possible to find a minimum by varying M_0, M_1, $M_{\rm K}$, and $p_{\rm K}$ simultaneously, very strong correlations appear and parameter configurations significantly deviate from ellipsoidal shapes, as shown in Fig. 7. This makes it difficult to draw regions in parameter space as is usually done, by considering configurations for which $\chi_i^2 < \chi_0^2 + \Delta\chi^2$, *and* to interpret them in terms of confidence levels—i.e.,

[3]More precisely, a "lower bound," not the minimum χ^2 in the mathematical sense.

[4]This value corresponds to a 2σ confidence level for varying four parameters, but we do not attempt to make such an interpretation in this particular case.

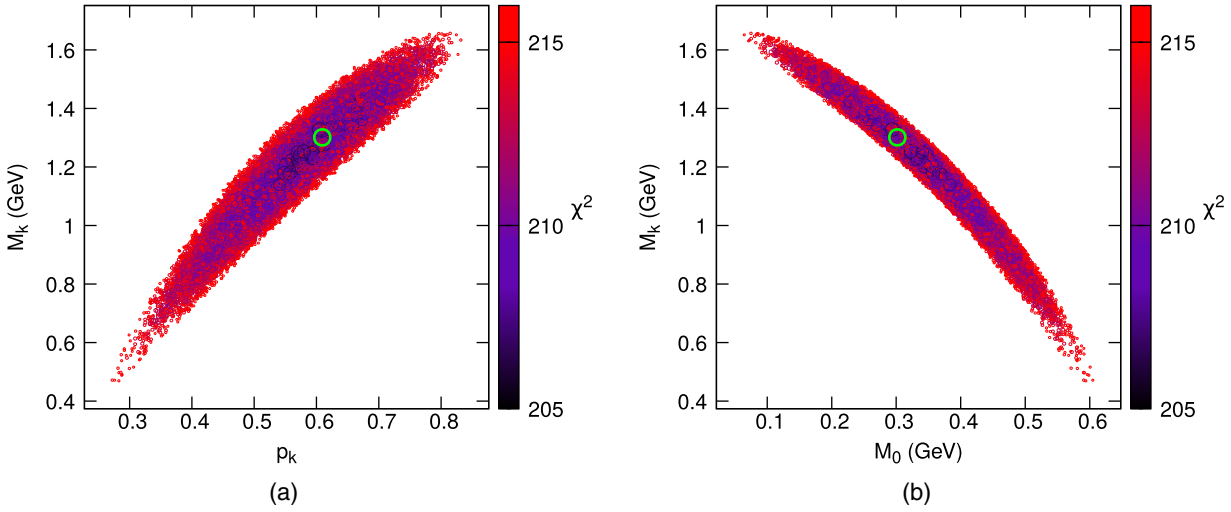

FIG. 7. Preliminary study of parameter space using model I for M_{D} and A for g_{K}; see Table IV, with fixed $p = 1.51$ and $q = 8$. The circles represent parameter configurations in a region where a minimum is found. The empty circles display the value of χ^2 both by color (as in palette) and by size (larger circles for smaller values of χ^2) for configurations with $\chi_i^2 < \chi_0^2 + \Delta\chi^2$, with $\Delta\chi^2 = 9.72$. This value of $\Delta\chi^2$ corresponds to a 2σ confidence level for varying four parameters simultaneously, in situations where the χ^2 as a function of parameters can be approximated as an ellipsoid around the minimum. In this case, however, such approximation is not valid, hindering an interpretation in terms of confidence levels. Strong correlations such as those shown likely indicate some "redundancy" in parameter space. (a) Correlation between M_{K} and p_{K}, where the green circle indicates the minimal configuration. (b) Correlation between M_{K} and M_0.

statistical errors of our analysis. As we will see in the next section, by varying only the three mass parameters M_0, M_1, and M_{K}, parameter space displays elliptical profiles for all correlations, allowing for a more sound statistical interpretation. It is interesting to note that the strong correlations appear also between M_{D} and g_{K} parameters, as seen in the right panel of Fig. 7.

The information regarding the values of p, q, and p_{K} is summarized in Table IV. We remark that these choices still allow for enough flexibility in our models.

Note that while we could have treated p_{K} as nuisance parameters, for our purposes it is enough to fix them to reasonable values, since we are mostly interested in addressing the compatibility of the asymptotic behavior of Eqs. (10), (14), and (15) with BELLE data; for this, it suffices to consider reasonable profile functions. A possible concern regards the estimation of statistical errors, which may be affected by fixing parameters. However, we remark that considering different models helps us in giving an estimate of some of the theoretical uncertainties of our extraction. All of our choices for models IA and IB are summarized in Table V.

2. Models IIA and IIB

Model II stems from different considerations—namely, we do not introduce the extra factor F, but rather assign a z_h dependence to the mass and power parameters of the Bessel function themselves, M and p. This offers a nice physical interpretation, especially if we recall that this b_{T} distribution originates as the Fourier transform of a power law, which resembles a propagator of the form $[M(z)^2 + q_T^2]^{-p(z)}$ in q_{T}-conjugate space. In this sense, the mass $M(z)$ can be regarded as an *effective mass*, which modifies the mass of the detected hadron M_h in a z_h-dependent way. The power $p(z)$ can be rewritten as $p(z) = 2 + \gamma_P(z)$, where the whole z_h dependence has been encoded into an *anomalous dimension* γ_P. As for model I, the strong correlations between $p(z)$ and $M(z)$ makes it impossible to extract them simultaneously in a converging fit; therefore, further constraints are required to

TABLE V. Minimal $\chi^2_{\mathrm{d.o.f.}}$ obtained by fitting models IA and IB, according to Table IV. In each case, we perform fits in the kinematical region of Eqs. (22) and (23). In both cases IA and IB, all dimensionless parameters are fixed, indicated in the table by an asterisk. Fixed values are as explained in Sec. III E.

$q_{\mathrm{T}}/Q < 0.15$ (pts = 168)		
	IA	IB
$\chi^2_{\mathrm{d.o.f.}}$	1.25	1.19
M_0(GeV)	$0.300^{+0.075}_{-0.062}$	$0.003^{+0.089}_{-0.003}$
M_1(GeV)	$0.522^{+0.037}_{-0.041}$	$0.520^{+0.027}_{-0.040}$
p^*	1.51	1.51
q^*	8	8
M_{K}(GeV)	$1.305^{+0.139}_{-0.146}$	$0.904^{+0.037}_{-0.086}$
p^*_{K}	0.609	0.229

be able to proceed with our analysis. For model II, we constrain the z_h behavior of $M_{\rm D}$ by analytically requiring that the theory lines appropriately reproduce some basic features of the measured cross section—namely, the peak height and the width of the P_T distributions—at each single measured value of the kinematic variable z_h. In particular [13], the width of the measured cross section reaches its maximum at intermediate values of z_h (around ∼0.6, as obtained in Ref. [13]) for all thrust bins belonging to the two-jet region. This property can be used as a constraint for the model with the help of a proper change of variables, that trades p and M for the width W and the peak height P,

$$p = \frac{1}{2}\left(\frac{3}{1-R} - 1\right), \qquad M = \frac{W}{z}\sqrt{\frac{3}{1-R}}, \tag{24}$$

where $W \geq 0$ and R is the ratio $P/P_{\rm max}$ between the peak height and its maximum possible value ($0 < R < 1$). The advantage of this operation is that R and W can be regarded as variables associated with the full cross section and not only with the TMD model. However, being a mere change of variables, this does not solve any correlation issues, which are simply being moved from (p, M) to (R, W). In particular, observation shows that R and W are inversely proportional with respect to their z_h dependence: where one shows a maximum, the other has a minimum, and vice versa. Therefore, we set

$$R = f(z_h, z_0), \qquad W = \frac{M_\pi}{f(z_h, z_0)^2}, \tag{25}$$

where $M_\pi = 0.14$ GeV is the mass of charged pions and f has to be a positive-definite function, never larger than 1 and with a minimum in $z_h = z_0$. This is where the information associated with the experimental observation comes into play, helping to select an appropriate z_h dependence for the TMD model. In fact, the function f has a minimum in the exact point where the width W has a maximum. One of the simplest functional forms which fulfills such requirements is

$$f(z, z_0) = 1 - (1-z)^\beta, \quad \text{with} \quad \beta = \frac{1-z_0}{z_0}. \tag{26}$$

This is what we adopt for model II. The expression of M_z and p_z in terms of $f(z)$ are summarized in Table IV.

Following the indication of these preliminary tests, we will focus on the study of the large-$b_{\rm T}$ (i.e., small-P_T) behavior of the fitted cross sections, leaving the exploration of the small-$b_{\rm T}$ region to further analyses. By large $b_{\rm T}$, here we mean "the largest $b_{\rm T}$ experimentally accessible," as the asymptotic behavior may not be so relevant for this dataset, as discussed in Sec. III B. For our main analysis with model II, we will adopt the functional forms of Eqs. (20) and (21), both characterized by two free parameters, $M_{\rm K}$ and $p_{\rm K}$. This gives two new models, which we label "IIA" and "IIB" (see Table IV).

We thus minimize χ^2 with respect to the free parameters $(z_0, M_{\rm K}, p_{\rm K})$ for models IIA and IIB. In these two cases, as for model I, we will estimate statistical errors by determining the 2σ confidence region in parameter space. Note that, while the parameter space shown in next section for model II has a distortion with respect to elliptical shapes, we have checked that rescaling the parameters allows us to correct for this. Nonetheless, we present results in terms of $(z_0, M_{\rm K}, p_{\rm K})$, since they are closely related to features of the data.

Following the above considerations, the main results of our analysis will be presented in the next subsection for all of our models.

F. Phenomenological results

With our final choices, we perform fits for each of the considered models, labeled IA, IB, IIA, and IIB, where "I" and "II" indicate the choice of parametrization for $M_{\rm D}$, while "A" and "B" indicate the model chosen for $g_{\rm K}$, according to the notation introduced in Table IV. In each case, we perform a χ^2-minimization procedure using MINUIT [51], fitting a total of three parameters in each model. We estimate parameter errors by considering 2σ confidence regions. In other words, for each model we consider configurations in parameter space around the minimal one, varying all parameters simultaneously and accepting those for which $\chi^2_i < \chi^2_0 + \Delta\chi^2$, with $\Delta\chi^2 = 8.02$; this value of $\Delta\chi^2$ is consistent with varying three parameters simultaneously. For statistical uncertainties, we perform fits with the central replica of the NNFFs in all cases. Final results for models IA and IB are reported in Table V. For models IIA and IIB, results are displayed in Table VI.

From a superficial look at Table V, one may conclude that the quality of model IB is higher, given the smaller values of $\chi^2_{\rm d.o.f.}$. However, we note that model IB has the disadvantage that the ellipsoidal approximation extends down to negative values of M_0, which must be excluded. This is reflected by the asymmetric errors in M_0 and $M_{\rm K}$ in the third column of Table V.

TABLE VI. Minimal $\chi^2_{\rm d.o.f.}$ obtained by fitting models IIA and IIB, according to Table IV. In each case, we perform fits in the kinematical region of Eqs. (22) and (23). There are no nuisance parameters in model II.

$q_{\rm T}/Q < 0.15$ (pts = 168)		
	IIA	IIB
$\chi^2_{\rm d.o.f.}$	1.35	1.33
z_0	$0.574^{+0.039}_{-0.041}$	$0.556^{+0.047}_{-0.051}$
$M_{\rm K}$(GeV)	$1.633^{+0.103}_{-0.105}$	$0.687^{+0.114}_{-0.171}$
p_k	$0.588^{+0.127}_{-0.141}$	$0.293^{+0.047}_{-0.038}$

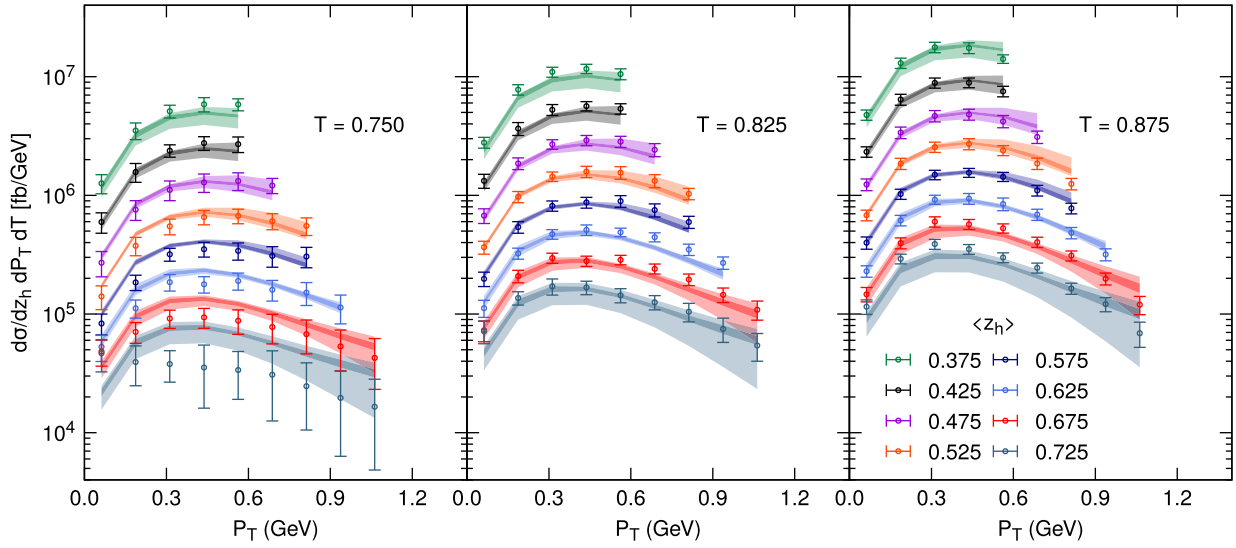

FIG. 8. Results of fitting model IA from Table IV to BELLE data on pion production from e^+e^- annihilation [13], in the kinematical region of Eqs. (22) and (23). Darker shaded bands represent the statistical uncertainty of the fit at a 2σ confidence level and correspond to the parameter configurations of Fig. 9. The lighter shaded bands are an estimate of the error induced by the collinear fragmentation functions used in the analysis, and they are produced by refitting the model function for each of the replicas provided by the NNFF NLO extraction of Ref. [33]. For a better visualization of results, central lines are not included, but they generally lie in the middle of the thin, darker statistical error bands. Models IB, IIA, and IIB give analogous results. We do not show them in the plot, as they would be indistinguishable.

Fits performed with model II have slightly higher χ^2's, as shown in Table VI. This is probably due to the fact that this model, being more tightly constrained, with only one free parameter controlling the z_h behavior of M_{D}, shows a limited flexibility compared to model I. Nonetheless, clear differences between models cannot be observed when comparing to data. We thus consider models I and II to be equally acceptable to describe the general profile of our functions M_{D} and g_{K}. We choose model IA to display the agreement of our predicted cross sections to the BELLE data in Fig. 8, noting that corresponding comparisons for models IB, IIA, IIB would indeed be very similar. Figure 8 shows two types of error bands: Darker bands represent the statistical uncertainty of the fit. The lighter bands are an estimate of the error induced by the collinear fragmentation functions used in the analysis. They are produced by refitting the model function for each of the replicas provided by the NNFF NLO extraction of Ref. [33].

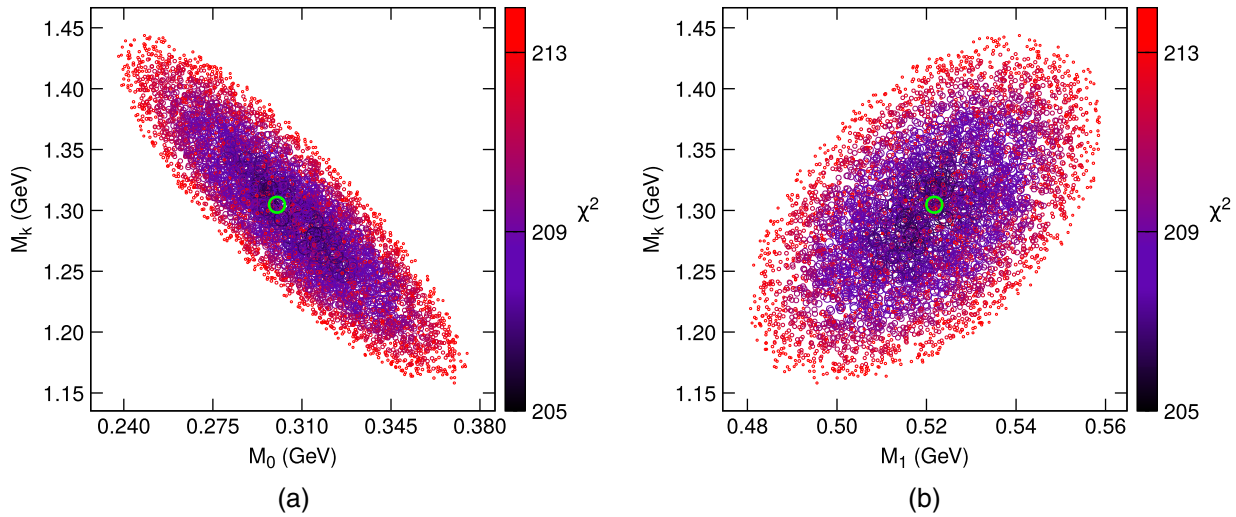

FIG. 9. 2σ confidence regions centered around the minimum configuration, shown in green, for the fit of model IA of Table IV in the kinematical region of Eqs. (22) and (23).

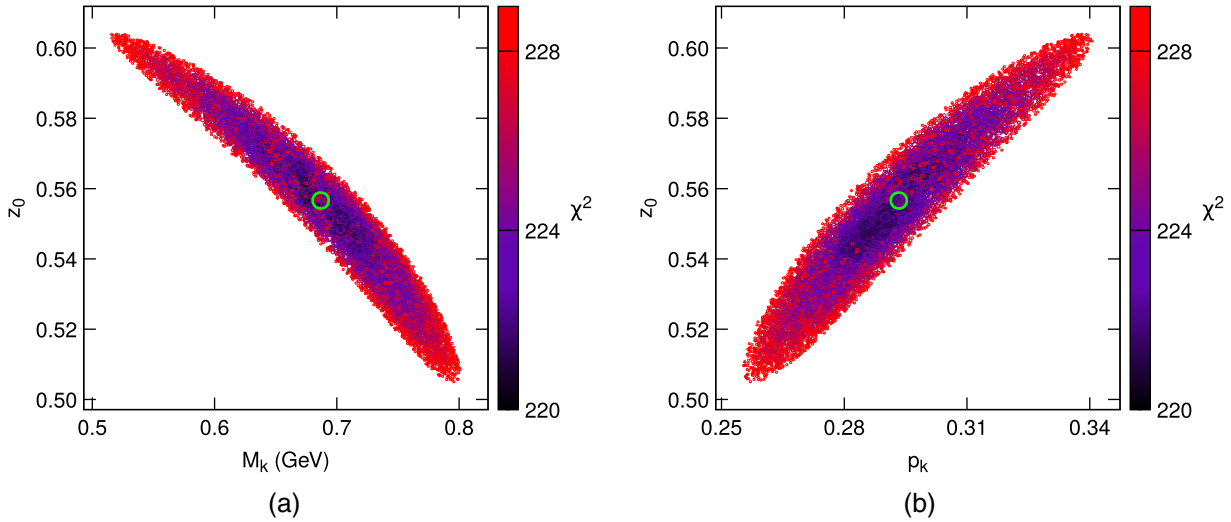

FIG. 10. 2σ confidence regions centered around the minimum configuration, shown in green, for the fit of model IIB of Table IV in the kinematic region of Eqs. (22) and (23). Here, the presence of some correlation among the free parameters controlling the behavior of M_{D} and g_{K} is signaled by a slight deformation from the expected ellipsoidal shapes.

For this estimate, only about 65% of the NNFF replicas allowed for a convergent fit.[5] A more detailed study of such errors is a necessity in this type of studies that need constraints from independent analyses. For now, we consider our estimate as a useful tool to understand the effect of the choice of collinear FFs in a TMD extraction. In fact, it is useful to observe in Fig. 8 that errors from the collinear functions are consistently larger than statistical errors. Arguably, the former render a more realistic picture of the precision at which TMDs can be extracted from data. It is clear from Fig. 8 that the quality of the description of data deteriorates at smaller values of T. This is not surprising, since the formalism employed [25,28,29] is expected to fail at smaller values of thrust, where the topology of the $e^+e^- \to hX$ events starts deviating from a two-jet-like configuration.

Further developments in the theoretical treatment of the interplay between the rapidity divergence regularization and the thrust dependence will likely improve the quality of the extraction by allowing the possible inclusion of more data points while achieving an improved agreement with data [25]. We leave this for future work [30].

Interesting results are found about $g_{\mathrm{K}}(b_T)$. We focus on the study of the large-b_{T} (i.e., small-P_T) behavior of the fitted cross sections, leaving to further analyses the exploration of the small-b_{T} region, on which we are unable to draw definite conclusions, as explained in Sec. III D. Our fit is rather sensitive to the modulation of g_{K} in the large-b_{T} region. Remarkably, it shows a strong preference for a sublinear power or logarithmic rising of g_{K}, while definitely ruling out the b_{T}^2 or b_{T}^4 behavior at large b_{T}. We stress that by large b_{T}, here we mean "the largest b_{T} experimentally accesible," as the asymptotic behavior may not be so relevant for this dataset, as discussed in Sec. III B.

It is important to understand the strength of correlations between M_{D} and g_{K} and the impact of model choices in the extraction of profile functions. Although these two points are not necessarily unrelated, we discuss them separately in what follows.

First, regarding correlations between M_{D} and g_{K} for a given model, in an ideal scenario one would expect them to be mild, which would provide some level of confidence when comparing results to other analyses or datasets.

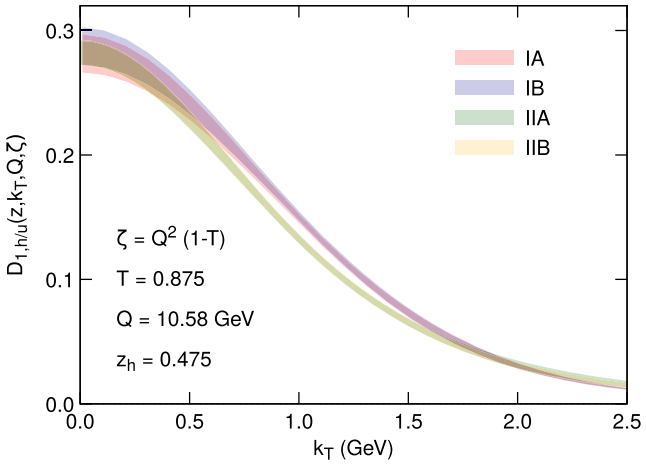

FIG. 11. Extractions of the unpolarized TMD FF, Eq. (3), from one-hadron production BELLE data of Ref. [13], using models IA, IB, IIA, and IIB of Table IV, in the kinematic region of Eqs. (22) and (23). The TMD FF for the $u \to \pi^+ + \pi^-$ channel is shown in momentum space.

[5]We checked that the uncertainty bands corresponding to this 65% span most of the uncertainties obtained with all of the NNFF sets.

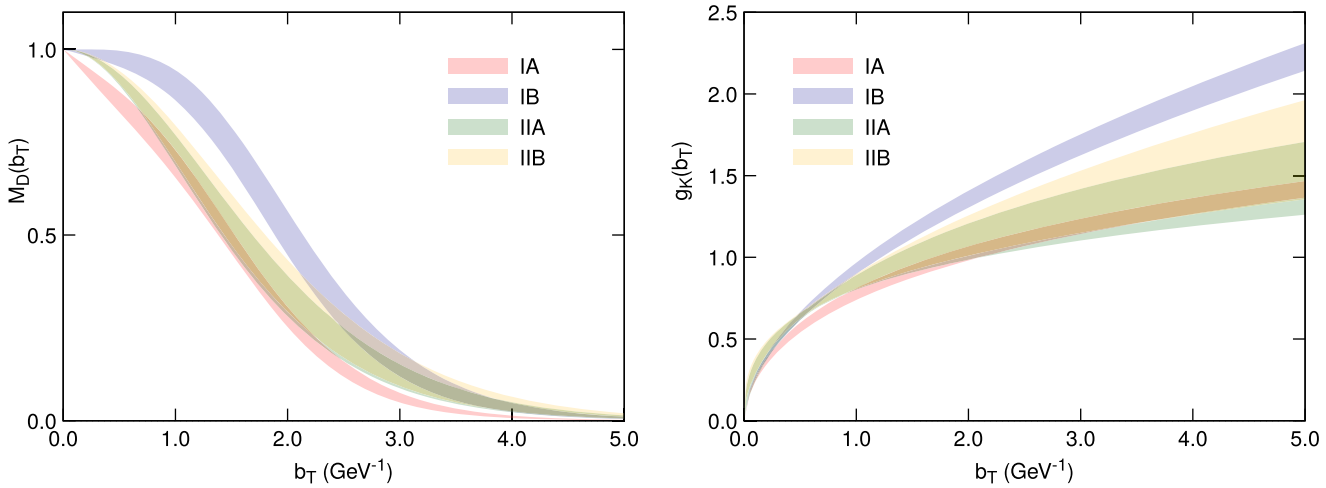

FIG. 12. Extractions of M_{D} and g_{K} in Eq. (3) from $e^+e^- \to hX$ BELLE data [13], in the kinematic region of Eqs. (22) and (23). In all cases, 2σ statistical error bands are shown. For model IA, they correspond to the region of parameter space of Fig. 9 while for model IIB, they correspond to that of Fig. 10. Left: M_{D} according to models IA, IB, IIA, and IIB of Table IV. Right: Corresponding results for g_{K}.

This situation is, however, not guaranteed. We find that in fact M_{D} and g_{K} are correlated, as shown in Fig. 9, where correlations between M_{K} and the mass parameters of M_{D}, M_0, and M_1 are displayed for model IA, and in Fig. 10, where analogous scatter plots are presented for model IIB, for the correlation of z_0 with M_{K} and p_{K}. We obtain analogous results for model IB, with the added feature that confidence regions in parameter space appear as ellipses truncated in the region $M_0 < 0$. For models of type II, the correlation between M_{D} and g_{K} appears to be stronger than in the parametrizations of type I, so much so that a slight residual deformation from the ellipsoidal form is still visible in Fig. 10, although the constraints intrinsically built in model I drastically limit the number of its free parameters. We checked that a transformation of parameters M_{K} and p_{K} render scatter plots with an approximate elliptical shape. It is noteworthy that the regions corresponding to the 2σ confidence level have well-defined contours, allowing for a reliable determination of the error affecting the extracted parameters.

Second, we find that the profile of the extracted functions strongly depends on model choices. Note that the full TMD in momentum space, shown in Fig. 11, shows differences beyond statistical error bands. Discrepancies are more visible when considering separately the results obtained for the extractions of M_{D} and g_{K}, as seen in Fig. 12, where the profile functions differ beyond statistical error bands. As such, those discrepancies should be considered as a kind of theoretical error. While this is only a rough estimate of one kind of theoretical uncertainties, it makes the case that statistical uncertainties are generally not enough to asses the quality of an extraction. Even though this is especially the case in studies like the present one, where only one process is considered, it is a matter of concern even for global fits.

We now compare our results against other recent TMD analyses. Since the relevant TMD FF in our studies is different from that of the usual CSS, SCET, and related treatments [see Eq. (5a)], we can only compare our results for the CS kernel, which, up to trivial constant factors, is the same in each scheme. In Fig. 13, we plot the CS kernel [6,50] computed to NLL accuracy:

$$\tilde{K}(b_{\mathrm{T}};\mu) = \frac{1}{2}\left[g_1^{\mathrm{K}}(\lambda) + \frac{1}{L_b^*} g_2^{\mathrm{K}}(\lambda)\right] - \frac{1}{2} g_K(b_T), \qquad (27)$$

where the functions g_1^{K} and g_2^{K}, which depend only on the combination $\lambda = 2\beta_0 a_S(\mu) L_b^*$, with $L_b^* = \log(\mu/\mu_{b_*})$, are reported in the Appendix. Our extraction of the CS kernel for all our models is compared to the results obtained in the analyses of PV19 [4] and SV19 [47].[6] For clarity, we do not show central lines, but only error bands in each case. Figure 13 shows a good agreement between our extraction of the CS kernel and the SV19 analysis in the region just above $b_{\mathrm{T}} \sim 2$ GeV^{-1}. Note that these two extractions are based on different factorization schemes and exploit different datasets.[7] The large-b_{T} behavior of our extraction is clearly different from the PV19 results, which adopts a b_{T}^4 asymptotic behavior in order to describe Drell-Yan production data from different experiments on a very wide kinematic range, and up to extremely high energies.

[6]Note that for the CS kernel, PV19 follows the conventions of Ref. [6]; the SV19 results must be multiplied by a factor of -2, and ours should be divided by a factor of 2.

[7]At this point, we can give a more quantitative indication of what we mean by large and small b_{T} values. When we talk about small b_T, we refer to values much smaller than $b_T^{\max}$, typically around 0.2–0.5 GeV^{-1}. Conversely, large b_T's are considered to be values much larger than $b_T^{\max}$—say, larger than 2 GeV^{-1}.

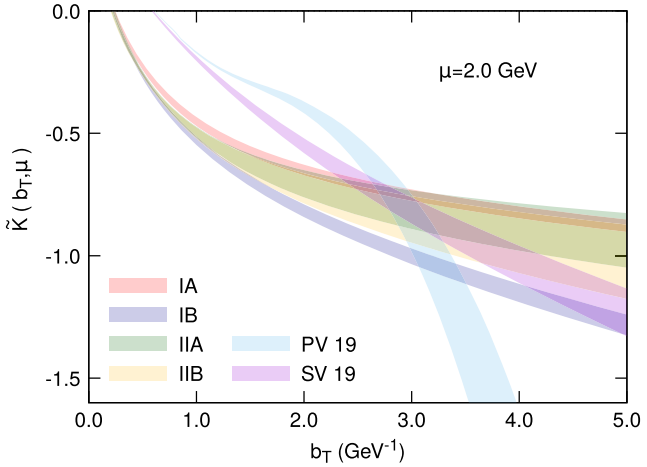

FIG. 13. Extractions of the CS kernel obtained in this analysis with models IA, IB, IIA, and IIB are compared with the PV19 [4] and SV19 [47] extractions. For clarity, central lines are not shown. While there is a good agreement between the linear and sublinear large-b_T behavior of this extraction and Ref. [47], the result of Ref. [4] shows an evident deviation at large b_T, where g_K goes like b_T^4. Discrepancies at small b_T are due to the higher pQCD accuracy of the PV19 and SV19 analyses. We also note that our models are essentially different at small b_T compared to those used in Refs. [4,47], as explained in the text.

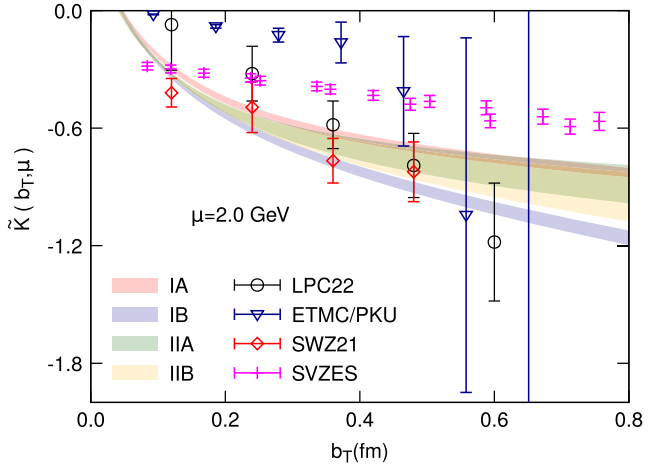

FIG. 14. The CS kernels obtained in this analysis by adopting models IA, IB, IIA, and IIB are compared to the CS kernel computed in lattice QCD in Refs. [54–57], at $\mu = 2$ GeV. For clarity, central lines for our extractions are not shown, and we display only the most recent lattice calculation for each group. The logarithmic- and sublinear-power large-b_T behavior assumed for our extraction seem to be well supported by lattice QCD estimations of the CS kernel.

Instead, in the small-b_T region, our extraction of the CS kernel differs from both PV19 and SV19 results, where the perturbative part of the CS kernel is expected to dominate, making all bands coincide.

This is mostly due to two factors. The first is the behavior of our model for g_K at small distances—it approaches zero only as b_T^p, with $0 < p < 1$, significantly more slowly compared to the b_T^2 behavior of the PV19 and SV19 parametrizations also at small distances. In fact, the effects of our extractions for g_K are still significant at relatively small values of b_T. Second, the approximations of Eq. (3) are likely not optimal to describe the small-b_T behavior of the TMDFF. Future improvements in the perturbative accuracy and a better treatment of the thrust dependence could resolve these discrepancies with respect to the results of the PV19 and SV19 analyses.

Recently, several lattice QCD calculations of the CS kernel have been performed by different groups and reported in Refs. [52–57]; it is therefore interesting to compare our extraction to some of these computations. We do this in Fig. 14, where for clarity we compare error bands of all our models with the most recent calculation of each lattice QCD collaboration [54–57]. The logarithmic- and sublinear-power large-b_T behavior assumed for our extractions seem to be well supported by lattice QCD estimations of the CS kernel. We note that while our results are in better agreement with the SWZ21 [56] and LPC22 [57] calculations, the general trend of our extractions is also consistent with the ETMC/PKU [55] and SVZES [54] results, characterized by a slow variation of the CS kernel at large b_T. Once again, we underline that in our analysis, little can be said about the small-b_T behavior of the CS kernel; thus, we focus our attention on the large-b_T regime, where BELLE experimental data offer good coverage.

IV. CONCLUSIONS

We performed an analysis of recent BELLE data for one-hadron production in e^+e^- annihilation [13] and extracted the TMD FF following the newly developed formalism of Ref. [25,28,29]. In this framework, the short-distance behavior of the TMD FF is constrained by collinear FFs, as in the standard CSS and SCET formalisms, while the long-distance behavior requires the parametrization and determination, via comparison to data, of two functions, M_D and g_K. We introduced constraints for these functions in the asymptotically large region of b_T, consistently with previous theoretical results from Refs. [44,48,49,58]. Our analysis is based on a maximum-likelihood procedure, carried out by χ^2 minimization. Statistical errors are estimated by a standard determination of confidence regions at the 2σ level.

Upon testing how different choices of available collinear FFs perform when compared to data, we found that both JAM20 [35] and NNFF [33] sets, although showing non-negligible differences (at least in some specific regions of z_h and b_T), are consistent with the P_T-dependent BELLE cross sections, within our approach.

For our extraction, constraints for both M_D and g_K in the asymptotically large-b_T region were imposed. For M_D, we considered models characterized by an exponential

asymptotic b_T decay, according to previous theoretical results from Refs. [44,58] and argued that, for consistency with universality of the large-distance behavior of TMDs, the CS kernel should grow more weakly than a linear function of b_T in the asymptotic limit. We considered two models for g_K satisfying that condition, which follow a sublinear power and a logarithmic behavior, as suggested in Refs. [49] and [48], respectively, in this limit. We showed that, in the considered kinematic region, all aforementioned constraints imposed in the very large b_T range are consistent with the data. We remark, however, that the asymptotic behavior of different models plays a role in extending results to smaller scales, and that the slow evolution characteristic of the region of a few GeV can be accommodated by the type of models we tested in this work (see detailed discussion in Ref. [44]).

A remarkable result of this analysis is the insight of the influence of the profile function of g_K in the region of intermediate moderate values of b_T, which we expect to be accessible at BELLE kinematics. Compared to previous studies [4,47], which gave indications on the preferred behavior of g_K at small b_T, our analysis based on the BELLE data, which correspond to a relatively moderate scale $Q = 10.6$ GeV, shows a significant sensitivity to larger values of b_T. We find clear signals that a b_T^2 or b_T^4 functional form is inappropriate to describe the long-distance behavior of the CSS kernel. In fact, the analyzed data show a definite preference for a logarithmic or sublinear modulation at large b_T, in line with the studies of Refs. [49,50] based on more general formal considerations.

The large-b_T behavior of our models, supplemented with constraints from BELLE data, seems to be well supported by the lattice determinations of the CS kernel from quasi-TMD wave functions [54–57], which evidence the slow variation of the kernel in this region of b_T. Remarkably, our extractions are in very good agreement with the calculations of Refs. [56,57] where an NLO matching is applied. This is a very important cross check, as lattice QCD calculations are based on totally different and independent methodologies.

On the other hand, little can be inferred from this analysis about the small-b_T behavior of the CS kernel and of g_K. This might be at least partially due to the relatively low energy of the BELLE experiment, but this is an issue which deserves more extensive studies, including higher accuracy in the perturbative expansion. A more rigorous formal treatment will be presented in Ref. [30].

A very important theoretical consideration regards the transition between short- and long-distance behavior, which should be carefully treated when embedding models into the type of TMD FF definition like that of Eq. (3), where the small-b_T behavior is, in principle, constrained by collinear factorization. In general, such constraints are not guaranteed unless models are optimally embedded, especially at small and moderate scales. Recently, this and related issues have been comprehensively addressed in Ref. [59] where, based on theoretical considerations, a practical recipe for phenomenology was provided that allows a more reliable combination of models of nonperturbative behavior into the CSS formalism. These considerations will likely help to resolve some of the issues we found at small b_T in our analysis. We plan to pursue these techniques in future work.

Another relevant aspect concerns the estimation of the errors affecting the phenomenological extraction of TMDs from experimental data. It is important to stress that while statistical errors do provide insight into the precision with which TMDs can be extracted, theoretical errors also play an important role, which remarkably affects accuracy. We addressed two sources of such errors and provided rough estimates of their size. First, we considered the effect that the statistical errors of the collinear functions have in the extraction of the unpolarized TMD FF by refitting our model with each one of the sets provided by the NNFF Collaboration. Second, the use of two different models for g_K allowed us to assess how profile functions extracted depend on model choices, as seen in Fig. 12. In both cases, our estimates are meant to provide examples of how important it is to perform error estimation beyond statistical uncertainties. More work is needed in order to address these issues with a more robust approach.

A possible future improvement in our analysis regards the treatment of experimental errors. For our work, we added in quadrature all errors provided by the BELLE Collaboration which may be a matter of concern, especially regarding correlated systematic errors, since they should be treated on a different footing. This can be done, for instance, by introducing nuisance parameters in the χ^2 statistic, in the form of a shift to theoretical estimates. This, however, likely requires more detailed information about the different sources of correlated systematic uncertainties. In our case, attempting to employ such methodology resulted in large values of the minimal χ^2, although it rendered almost identical results in the profile functions.

Although our analysis was carried out on a rather limited subset of the BELLE data, we consider this work an essential first step. We stress that, to the best of our knowledge, this is the only phenomenological analysis where the thrust dependence of the cross section is explicitly taken into account and well described over three different bins. Other studies [12,60] resort to a combination of the thrust bins, resulting in a cross section which is some sort of average over thrust, or they simply integrate it over. Extending our results to a wider range of thrust and z_h bins requires further formal developments on identifying and extending the optimal kinematic region where the TMD formalism developed for Region 2 in $e^+e^- \to hX$ can be successfully applied [25,45]. Moreover, the connection between the regularization of the rapidity divergences and the thrust dependence must be set on a more solid

formal ground, as it crucially affects the correlation among T, P_T, and z_h. This will likely improve the quality of the extraction by allowing us to possibly include more data points while achieving an even better agreement with data [30].[8]

ACKNOWLEDGMENTS

We thank Ted Rogers for useful discussions regarding formal aspects of the CS kernel. We are grateful to Alexey Vladimirov for making available to us the results of the SV19 extraction and the SVZES lattice calculation of the CS kernel, and to Andrea Signori for providing results of the PV19 fit. We thank Xu Feng, Michael Wagman, and Qi-An Zhang for interesting discussions on their lattice QCD determination of the Collins-Soper kernel and for providing us with relevant recent results on the subject.

This project has received funding from the European Union's Horizon 2020 research and innovation program under Grant Agreement No. 824093.

APPENDIX: WILSON COEFFICIENTS AND g_i FUNCTIONS

In this appendix, we provide the explicit expression of the quantities necessary to compute the perturbative part of the TMD FF. The one-loop Wilson coefficients $\mathcal{C}^{[1]}(z) \equiv \mathcal{C}^{[1]}(z, b_*; \mu_{b_*}, \mu_{b_*}^2)$ appearing in Eq. (3) are calculable in pQCD and are given by [6]

$$z^2\mathcal{C}^{[1]}_{q/q}(z) = 2C_F\left(1 - z + 2\frac{1+z^2}{1-z}\log z\right) - C_F\frac{\pi^2}{6}\delta(1-z), \tag{A1}$$

$$z^2\mathcal{C}^{[1]}_{g/q}(z) = 2C_F\left[z + 2\frac{1+(1-z)^2}{z}\log z\right]. \tag{A2}$$

To reach NLL accuracy, the anomalous dimension γ_K of the soft kernel is expanded up to two loops, while all other quantities are written to one loop. The functions g_i, $i = 1, 2$ and g_j^K, $j = 2, 3$, required to reach NLL accuracy in the expression of the TMD FF of Eq. (3), depend on the variable $\lambda = 2\beta_0 a_S(Q)\log\frac{Q}{\mu_{b_*}}$ and are given by [29]

$$g_1(\lambda) = \frac{\gamma_K^{[1]}}{4\beta_0}\left(1 + \frac{\log(1-\lambda)}{\lambda}\right), \tag{A3}$$

$$g_2(\lambda) = \frac{\gamma_K^{[1]}}{8\beta_0^2}\frac{\beta_1}{\beta_0}\frac{\lambda}{1-\lambda}\left(1 + \frac{\log(1-\lambda)}{\lambda} + \frac{1}{2}\frac{1-\lambda}{\lambda}\log^2(1-\lambda)\right) - \frac{\gamma_K^{[2]}}{8\beta_0^2}\left(\frac{\lambda}{1-\lambda} + \log(1-\lambda)\right) - \frac{\gamma_d^{[1]}}{2\beta_0}\log(1-\lambda), \tag{A4}$$

$$g_1^K(\lambda) = \frac{\gamma_K^{[1]}}{2\beta_0}\log(1-\lambda), \tag{A5}$$

$$g_2^K(\lambda) = \frac{\gamma_K^{[1]}}{4\beta_0^2}\frac{\beta_1}{\beta_0}\frac{\lambda^2}{1-\lambda}\left(1 + \frac{\log(1-\lambda)}{\lambda}\right) - \frac{\gamma_K^{[2]}}{4\beta_0^2}\frac{\lambda^2}{1-\lambda}, \tag{A6}$$

with

$$\gamma_K^{[1]} = 16C_F, \tag{A7a}$$

$$\gamma_K^{[2]} = 2C_A C_F\left(\frac{536}{9} - \frac{8\pi^2}{3}\right) - \frac{160}{9}C_F n_f, \tag{A7b}$$

where n_f is the total number of fermion fields considered, while β_0 and β_1 are the coefficients of the beta functions up to two loops:

$$\beta_0 = \frac{11}{3}C_A - \frac{2}{3}n_f, \tag{A8a}$$

$$\beta_1 = \frac{34}{3}C_A^2 - \frac{10}{3}C_A n_f - 2C_F n_f. \tag{A8b}$$

We refer to Ref. [50] for the explicit values of the anomalous dimensions, the Collins-Soper kernel, and the QCD beta function coefficients, having taken care of multiplying by 2 all the coefficients related to the CS kernel.

[8] Recently, a new analysis by the Pavia group has been made available [61].

[1] M. Anselmino, M. Boglione, U. D'Alesio, S. Melis, F. Murgia, and A. Prokudin, Phys. Rev. D **87**, 094019 (2013).
[2] A. Signori, A. Bacchetta, M. Radici, and G. Schnell, J. High Energy Phys. 11 (2013) 194.
[3] A. Bacchetta, F. Delcarro, C. Pisano, M. Radici, and A. Signori, J. High Energy Phys. 06 (2017) 081; 06 (2019) 051(E).
[4] A. Bacchetta, V. Bertone, C. Bissolotti, G. Bozzi, F. Delcarro, F. Piacenza, and M. Radici, J. High Energy Phys. 07 (2020) 117.

[5] M. G. Echevarria, I. Scimemi, and A. Vladimirov, J. High Energy Phys. 09 (2016) 004.
[6] J. Collins, *Foundations of Perturbative QCD* (Cambridge University Press, Cambridge, England, 2011).
[7] S. M. Aybat and T. C. Rogers, Phys. Rev. D **83**, 114042 (2011).
[8] M. G. Echevarría, A. Idilbi, and I. Scimemi, Phys. Lett. B **726**, 795 (2013).
[9] A. Idilbi, X.- d. Ji, J.-P. Ma, and F. Yuan, Phys. Rev. D **70**, 074021 (2004).
[10] M. Anselmino, M. Boglione, U. D'Alesio, J. O. Gonzalez Hernandez, S. Melis, F. Murgia, and A. Prokudin, Phys. Rev. D **92**, 114023 (2015).
[11] M. Anselmino, M. Boglione, U. D'Alesio, J. O. Gonzalez Hernandez, S. Melis, F. Murgia, and A. Prokudin, Phys. Rev. D **93**, 034025 (2016).
[12] U. D'Alesio, F. Murgia, and M. Zaccheddu, Phys. Rev. D **102**, 054001 (2020).
[13] R. Seidl *et al.* (Belle Collaboration), Phys. Rev. D **99**, 112006 (2019).
[14] M. Boglione, J. Gonzalez-Hernandez, and R. Taghavi, Phys. Lett. B **772**, 78 (2017).
[15] M. Soleymaninia and H. Khanpour, Phys. Rev. D **100**, 094033 (2019).
[16] M. Modarres and R. Taghavi, Phys. Rev. D **104**, 114004 (2021).
[17] W. Braunschweig *et al.* (TASSO Collaboration), Z. Phys. C **47**, 187 (1990).
[18] C. Berger *et al.* (PLUTO Collaboration), Z. Phys. C **22**, 103 (1984).
[19] A. Petersen *et al.*, Phys. Rev. D **37**, 1 (1988).
[20] D. K. Bhattacharjee, P. J. Cherian, and D. K. Maity, Phys. Rev. D **41**, 9 (1990).
[21] H. J. Behrend *et al.* (CELLO Collaboration), Z. Phys. C **14**, 189 (1982).
[22] M. G. Echevarria, A. Idilbi, and I. Scimemi, J. High Energy Phys. 07 (2012) 002.
[23] M. G. Echevarria, A. Idilbi, A. Schäfer, and I. Scimemi, Eur. Phys. J. C **73**, 2636 (2013).
[24] Y. Makris, F. Ringer, and W. J. Waalewijn, J. High Energy Phys. 02 (2021) 070.
[25] M. Boglione and A. Simonelli, J. High Energy Phys. 02 (2022) 013.
[26] Z.-B. Kang, D. Y. Shao, and F. Zhao, J. High Energy Phys. 12 (2020) 127.
[27] L. Gamberg, Z.-B. Kang, D. Y. Shao, J. Terry, and F. Zhao, Phys. Lett. B **818**, 136371 (2021).
[28] M. Boglione and A. Simonelli, Eur. Phys. J. C **81**, 96 (2021).
[29] M. Boglione and A. Simonelli, J. High Energy Phys. 02 (2021) 076.
[30] M. Boglione and A. Simonelli, Thrust resummation and rapidity divergence regularization (to be published).
[31] J. C. Collins, D. E. Soper, and G. F. Sterman, Nucl. Phys. **B250**, 199 (1985).
[32] J. C. Collins, D. E. Soper, and G. F. Sterman, Adv. Ser. Dir. High Energy Phys. **5**, 1 (1989).
[33] V. Bertone, S. Carrazza, N. P. Hartland, E. R. Nocera, and J. Rojo (NNPDF Collaboration), Eur. Phys. J. C **77**, 516 (2017).
[34] U. D'Alesio, F. Murgia, and M. Zaccheddu, J. High Energy Phys. 10 (2021) 078.
[35] E. Moffat, W. Melnitchouk, T. C. Rogers, and N. Sato (Jefferson Lab Angular Momentum (JAM) Collaboration), Phys. Rev. D **104**, 016015 (2021).
[36] A. Buckley, J. Ferrando, S. Lloyd, K. Nordström, B. Page, M. Rüfenacht, M. Schönherr, and G. Watt, Eur. Phys. J. C **75**, 132 (2015).
[37] M. Boglione, J. O. Gonzalez Hernandez, S. Melis, and A. Prokudin, J. High Energy Phys. 02 (2015) 095.
[38] J. Collins, L. Gamberg, A. Prokudin, T. C. Rogers, N. Sato, and B. Wang, Phys. Rev. D **94**, 034014 (2016).
[39] J. O. Gonzalez-Hernandez, T. C. Rogers, N. Sato, and B. Wang, Phys. Rev. D **98**, 114005 (2018).
[40] B. Wang, J. O. Gonzalez-Hernandez, T. C. Rogers, and N. Sato, Phys. Rev. D **99**, 094029 (2019).
[41] M. Boglione, J. Collins, L. Gamberg, J. Gonzalez-Hernandez, T. Rogers, and N. Sato, Phys. Lett. B **766**, 245 (2017).
[42] M. Boglione, A. Dotson, L. Gamberg, S. Gordon, J. Gonzalez-Hernandez, A. Prokudin, T. Rogers, and N. Sato, J. High Energy Phys. 10 (2019) 122.
[43] M. Boglione, M. Diefenthaler, S. Dolan, L. Gamberg, W. Melnitchouk, D. Pitonyak, A. Prokudin, N. Sato, and Z. Scalyer (Jefferson Lab Angular Momentum (JAM) Collaboration), J. High Energy Phys. 04 (2022) 084.
[44] J. Collins and T. Rogers, Phys. Rev. D **91**, 074020 (2015).
[45] M. Boglione, J. O. Gonzalez-Hernandez, and A. Simonelli, SciPost Phys. Proc. **8**, 139 (2022).
[46] I. Scimemi and A. Vladimirov, Eur. Phys. J. C **78**, 89 (2018).
[47] I. Scimemi and A. Vladimirov, J. High Energy Phys. 06 (2020) 137.
[48] C. Aidala, B. Field, L. Gamberg, and T. Rogers, Phys. Rev. D **89**, 094002 (2014).
[49] A. A. Vladimirov, Phys. Rev. Lett. **125**, 192002 (2020).
[50] J. Collins and T. C. Rogers, Phys. Rev. D **96**, 054011 (2017).
[51] F. James and M. Roos, Comput. Phys. Commun. **10**, 343 (1975).
[52] P. Shanahan, M. Wagman, and Y. Zhao, Phys. Rev. D **102**, 014511 (2020).
[53] Q.-A. Zhang *et al.* (Lattice Parton Collaboration), Phys. Rev. Lett. **125**, 192001 (2020).
[54] M. Schlemmer, A. Vladimirov, C. Zimmermann, M. Engelhardt, and A. Schäfer, J. High Energy Phys. 08 (2021) 004.
[55] Y. Li *et al.*, Phys. Rev. Lett. **128**, 062002 (2022).
[56] P. Shanahan, M. Wagman, and Y. Zhao, Phys. Rev. D **104**, 114502 (2021).
[57] M.-H. Chu *et al.* (LPC Collaboration), Phys. Rev. D **106**, 034509 (2022).
[58] P. Schweitzer, M. Strikman, and C. Weiss, J. High Energy Phys. 01 (2013) 163.
[59] J. O. Gonzalez-Hernandez, T. C. Rogers, and N. Sato, Phys. Rev. D **106**, 034002 (2022).
[60] Z.-B. Kang, X. Liu, F. Ringer, and H. Xing, J. High Energy Phys. 11 (2017) 068.
[61] A. Bacchetta, V. Bertone, C. Bissolotti, G. Bozzi, M. Cerutti, F. Piacenza, M. Radici, and A. Signori, arXiv: 2206.07598.